Fe-Modified Pd as an Effective Multifunctional Electrocatalyst for Catalytic Oxygen Reduction and Glycerol Oxidation Reactions in Alkaline Media

Andrea Cassani, Nazym Tuleushova, Qing Wang, Hazar Guesmi, Valérie Bonniol, Julien Cambedouzou, Sophie Tingry, Mikhael Bechelany, David Cornu, Yaovi Holade

Fe-Modified Pd as an Effective Multifunctional Electrocatalyst for Catalytic Oxygen Reduction and Glycerol Oxidation Reactions in Alkaline Media

Andrea Cassani,[1,‡] Nazym Tuleushova,[1,‡] Qing Wang,[2] Hazar Guesmi,[2] Valerie Bonniol,[1] Julien Cambedouzou,[1] Sophie Tingry[,1], Mikhael Bechelany,[1] David Cornu,[*,1] and Yaovi Holade[*,1]*

[1]Institut Européen des Membranes de Montpellier, IEM, UMR 5635, Univ Montpellier, ENSCM, CNRS, 34090 Montpellier, France

[2]Institut Charles Gerhardt de Montpellier, ICGM, UMR 5253, Univ Montpellier, ENSCM, CNRS, 34090 Montpellier, France.

KEYWORDS. Palladium nanoparticles; reduced graphene oxide; oxygen reduction reaction; glycerol electrooxidation reaction; DFT calculations.

ABSTRACT. The development of high-performance catalytic nanomaterials is important to implement sustainable any electrochemical energy device of alkaline fuel cell, metal-air battery and electrolyzers in the envisaged energy transition scenarios. Synthesizing nanocatalysts to effective as both anode materials for oxidation of glycerol (by-product of

biodiesel industry) and cathode materials for oxygen reduction (ORR) is still a bottleneck. Herein, we report palladium-based nanomaterials whose physicochemical and electrochemical properties are tuned by the judicious choice of the support (rGO, Vulcan XC72R), the addition of a co-element (Fe), and the structure (alloy/core-shell). The bimetallic-based electrode shows a drastically enhanced electrocatalytic performance with a beneficial shifting of the onset potential, production of high currents, and good durability for both ORR (kinetic current density j_k = 2 mA cm^{-2}_{Pd} or 1 A mg^{-1}_{Pd}), and glycerol oxidation (j_p = 2.3 mA cm^{-2}_{Pd} or 1.11 A mg^{-1}_{Pd} at the peak), higher than commercial catalyst and existing literature. The presents result findings also provide news fundamental insights about the accurate measurement of the kinetic metrics of ORR by employing a rotating disk (-ring) electrode (R(R)DE) setup in alkaline electrolytes at metallic catalysts. Indeed, the anodic scanning of the electrode from the low potential to the high one results in an ultrafast electrochemical kinetics with a positive shift of the half-wave potential of $\Delta E_{1/2,anodic/cathodic}$ = 60 mV from the cathodic direction to the anodic one. The kinetic current density dramatic increases, $j_{k,anodic}$ = 19.0×, 6.9×, 3.4×, and 2.4×$j_{k,cathodic}$ at 950, 900, 870, and 850 mV_{RHE}, respectively. The advantage of the synthesis methodology relies on the non-use of organic molecules as capping and surfactant in order to produce bare (ligand-free) bimetallic PdFe electrocatalysts with clean catalytic surface in a facile and straightforward way.

1. Introduction

The development of a multifunctional catalytic material capable of functioning as anode and cathode in basic media is particularly essential for simplifying and reducing the cost of the electrochemical converters (production and storage of the energy) of fuel cells (FCs), metal-air batteries, and electrolyzers. Specifically, the study of the catalytic electro-oxidation of biomass-derived compounds (ethanol, glycerol, and carbohydrates) has gained tremendous

interest in the last decade for the neutral-carbon processes of electricity production in low temperature fuel cells, CO_2 electro-conversion, and green H_2 production with low energy input electrolyzers.[1-2] Among those organics, glycerol is the most attractive because it is not only a sustainable method for recovering waste from industrial processes of biodiesel and soap production, but also a cogeneration pathway to electro-synthesize high value-added chemicals, thereby contributing to the reduction of overall costs.[1] On the other side, achieving the maximum faradaic efficiency and speeding up the low electrochemical kinetics of the oxygen reduction reaction (ORR), a common process for fuel cells and metal-air batteries, are central aspects for sustainable electrochemical energy conversion.[3-4] However, there is currently a strong lack of a catalytic material that catalyzes at high current densities both glycerol oxidation reaction in the anode range of 0.25-0.75 V_{RHE} and ORR at the cathode potential of 0.95-0.75 V_{RHE} while achieving the threshold of $4e^-$ (maximum faradaic efficiency). Indeed, given that the operating cell voltage is $U = E_{(cathode)} - E_{(anode)}$, a low potential is sought for the glycerol oxidation but the opposite for ORR.

Seminal studies have shown that the short-list of metals that are likely to enable the aforementioned functional compromise is composed of Pt and Pd.[5-6] The addition of abundant *d*-block metals (Fe, Sn, Mn, Bi, Ni, and Ag) to noble metals of Pt, Pd, and Au is a strong means of significantly reducing the precious metal quantity and synergistically increasing the electrocatalytic indicators of performance during the oxidation of glycerol in alkaline media.[7-10] Recently, a number of reports have revealed that high electrocatalytic performance could be achieved at those types of nanocatalysts, i.e., E_{onset} = 0.2-0.6 V_{RHE} at the onset and j_p = 2-5 mA cm^{-2}_{metal} (1-18 A mg^{-1}_{metal} and 50-300 mA cm^{-2}_{geo}) at the peak.[8,10-12] Pd-based nanostructured materials that provide similar or even better ORR performance than those based on Pt in basic electrolytes are the best compromise for both processes of ORR and glycerol oxidation. Quantitatively, rotating disk/ring electrode (RDE/RRDE, 1600

rpm) studies showed that the half-wave potential of ORR is enhanced ($E_{1/2}$ = 0.87-0.95 V_{RHE}) and the mass transport-free kinetic current density j_k = 0.5-11.6 mA cm^{-2}_{metal} = 0.5-16.4 A mg^{-1}_{metal} in 0.1 M KOH.[13-17] However, there are currently no comprehensive studies about the multifunctional ability of those high-performance materials, i.e., simultaneous use of the same material for ORR and the electrooxidation of organics in aqueous alkaline electrolytes.

Shinozaki *et al.*[18] have demonstrated that, in 0.1 M $HClO_4$ electrolyte, the scan direction of the potential affects strongly the measured activity of ORR. It was specifically observed that for a fixed electrode potential interval of -10 to 1000 mV_{RHE} at 0.005 V s^{-1}, $j_{k,anodic}$ for the anodic sweep is significantly higher than that of the cathodic sweep ($j_{k,cathodic}$). For instance, at 0.9 V_{RHE}, $j_{k,anodic} = 5.3 \times j_{k,cathodic}$ and $j_{k,anodic} = 2.4 \times j_{k,cathodic}$ for bulk and nanoscale Pt, respectively.[18] It was argued that the observed trend is related to the beginning of the ORR, which leads to a higher performance when it starts in the zone where the surface of Pt is exempt of oxides. As the ORR process is radically different from acidic to basic solutions, it is necessary to question whether this conclusion holds in an alkaline environment where Pd is expected to be the benchmarked nano-electrocatalyst. This is particularly important to allow a fair comparison of the performance of new classes of nano-electrocatalysts. Indeed, while the scan direction is clearly indicated in some cases to be the cathodic direction (from higher to lower value, 1.1 to 0.3 V_{RHE}[19]) or the anodic direction (from lower to higher potential, 0.06/0.2 to 1.1 V_{RHE}[20-21]), most of reports[15,22-24] do not state the scan protocol, which certainly leads to a conflicting comparison of the performance. Historically, for supported metal nanoparticles, the support (Vulcan carbon, graphene oxide based (GO, rGO/RGO), etc.) enables not only to reduce the metal loading to 10-50 wt.%, but also to improve the electrocatalytic performance through the metal-support interaction. It is nevertheless to be noted that the complexity of the utilized synthesis methods to produce nanocatalysts and the low cutting-edge performance levels of activity and durability do not allow tackling

sustainably the takeoff of the electrochemical converters in the present context of energy transition. Also, the development of computational methods to assist electrocatalysis in elucidating the performance trends as well as identifying new nanocatalysts is missing in the case of glycerol.

As aforementioned, Pd-Fe supported onto Vulcan or rGO was often applied to ORR and glycerol oxidation separately, which make the results difficult to compare because of different conditions of preparation/testing (synthesis including organic capping agents/surfactants), and the works dealing with the simultaneous evaluation of the electrocatalytic properties and DFT calculations are rarely available together. To address the above challenges with a single study by using bare (ligand-free) particles, we report a straightforward and convenient procedure to generate bare (ligand-free) iron-diluted palladium nanostructures and then to interrogate their electrocatalytic properties for ORR and glycerol oxidation in basic conditions. The integrated methods of electro-, and physicochemical characterization have shown that not only the presence of iron and the nature of the support for the supported nanomaterials of $Pd_{1-x}Fe_x$/Vulcan and $Pd_{1-x}Fe_x$/rGO (x = 0, 0.2) strongly affect the catalytic properties, but also, the bimetallic composition outperforms the monometallic materials and the tested commercial Pd/C. Moreover, DFT calculations on Pd(111) and Pd-Fe(111) extended surfaces reveal how the high stability of Fe on the sub-surface layer modifies the electronic properties of the surface Pd and enhances its activity toward glycerol oxidation. We have definitely evidenced how the non-disclosure of the scan direction during the recording of ORR polarization curves leads to an unfair assessment of the performance and so the incorrect comparison with existing data in the literature.

2. Experimental

2.1. Reagents and materials

Potassium hydroxide (KOH, 99.98%, (trace metal basis)) was purchased from Acros Organics. Potassium bromide (KBr, 99%), and potassium tetrachloropalladate (II) (K_2PdCl_4, Premion®, 99.99% (metals basis), Pd 32.2% min) were obtained from Alfa Aesar. Iron (II) acetate ($Fe(CH_3CO_2)_2$, ≥99.99% trace metals basis), hydrogen peroxide solution (H_2O_2, 30%), graphite powder (<20 μm), isopropanol (≥99.5%), Nafion® suspension (5 wt%), potassium nitrate (KNO_3, 99.0% min), sodium borohydride ($NaBH_4$, 99%), and potassium hexacyanoferrate ($K_3[Fe(CN)_6]$, ≥99.0%), potassium permanganate ($KMnO_4$, ≥99%), were obtained from Sigma-Aldrich. Sulfuric acid (H_2SO_4, 97%) was obtained from Honeywell. Phosphoric acid (H_3PO_4, 85%), and hydrochloric acid (HCl, 37%) were obtained from VWR. Pd/C (20 wt.%, 3-4 nm) was purchased from Premetek Co., USA. Membrane for filtration (0.2 μm) was obtained from Whatman. Those chemicals were utilized without any treatment. AvCarb MGL190 carbon paper electrode (190 μm thickness), and hydroxide anion exchange membrane (fumapem® FAA-3-50, 45-50 μm thickness) were obtained from Fuel Cell Store (US). The latter was soaked in NaOH (1 M, 24 h, room temperature) before use. Vulcan XC72R carbon black was provided by Cabot Corporation (Europe, Middle East & Africa; SIA Cabot Latvia, Latvia). Gases were ultrapure and purchased from Air Liquide (France), O_2 (grade 5.1), N_2 (grade 4.5), Ar (grade 5.0), and CO (type CO-N47). Ultrapure water (18.2 MΩ cm at 20 °C) was produced by a Milli-Q Millipore source (MQ).

2.2. Nanocatalysts preparation

Preparation of GO and rGO. GO was prepared by chemical oxidation and exfoliation of graphite under acidic condition according to the improved Hummers' method.[25] A typical synthesis of GO strictly follows the addition order of reagents as below (goal: avoid having too concentrated $KMnO_4$ in the acid solution that could become explosive). Typically, 3 g of

graphite were dissolved under stirring in an acid mixture of H_2SO_4, and H_3PO_4 at 360, and 40 mL, respectively. Then, 18 g of $KMnO_4$ were slowly poured in the previous solution (in ice bath). The reaction continued under stirring at 50 °C overnight. Then, the reaction was quenched by stopping the heating and was naturally left to cool to ambient temperature. After transferring in an ice bath, H_2O_2 (3 mL) was added under stirring. After 1 h, the mixture was centrifuged at 4000 rpm for 15 min. The successive washing by 30% HCl and DI water (each step is done by 10 min centrifugation at 4000 rpm) until obtaining a transparent supernatant (removed part) that produces a sticky precipitate of GO. rGO was obtained from GO by $NaOH/NaBH_4$ reduction.[26] Typically, GO (600 mg) was dissolved in ultrapure water (600 mL) with sonication, which lasts 2 h. After that, KOH (8 mol L^{-1}, 16 mL, 2 mL min^{-1} (syringe pump (KD Scientific)) was introduced and the preparation was stirred (10 min). Subsequently, under stirring, $NaBH_4$ (4.5 g) was gently poured in and the resulting batch was warmed up to 80 °C. After one hour of reaction under stirring, rGO was finally recovered through filtering on a Buchner system, copious washing (5 times) by MQ water and drying in oven overnight.

Thermal treatment of Vulcan XC72R carbon black. The as-received material underwent a thermal treatment (activation) as per our earlier method.[27] Basically, a Pyrex crucible with 2 g of the commercial material was put in a furnace and heated to 400 °C (5 °C min^{-1}, N_2). After four hours of operation, the furnace was subsequently left to cool down to ambient temperature. Hereafter, the as-received material was referred to as Vuclan-p ("p" for "pristine") and the pre-treated material termed to as Vulcan.

Synthesis of Pd-based nanoelectrocatalysts. Four types of materials, $Pd_{1-x}Fe_x$/Vulcan and $Pd_{1-x}Fe_x$/rGO (x = 0, 0.2), at the targeted metal loading of 20 wt.% were fabricated by the bromide anion exchange (BAE) method in which KBr act as the organic-free complexing agent,[19] but with modifications. The advantage is to avoid the use of organic molecules as

capping and surfactant agents, which will enable to produce bare (ligand-free) bimetallic PdFe electrocatalysts with clean catalytic surface because remaining trace of surfactants limit access to some active sites. To synthesize 100 mg of catalyst, suitable proportions of each individual metallic precursor were solubilized with MQ water (100 mL, 25 °C, and magnetic agitation). After adding KBr (n(KBr)/n(metals) = 100), the mixture was transferred in a Elmasonic sonication system (Grosseron, France). Then, 80 mg of the support was added and ultrasonic mixing was carried out for 45 min. Thereafter, the mixture was raised to 40 °C and $NaBH_4$ (0.1 M, 15 mL) was further added at 2 mL min^{-1} (syringe pump (KD Scientific)). After 2 h of reaction, the supported nanocatalysts were recovered following filtering through Buchner system, copious washing with water before drying in an oven (40 °C, 12 h).

2.3. Physicochemical characterization

Elemental analysis was done an Agilent 5110 VDV spectrometer, inductively coupled plasma optical emission spectrometry (ICP-OES). A FEG JEOL 2200FS microscope (200 kV) was utilized for energy-dispersive X-ray (EDX), and scanning transmission electron microscopy (S/TEM) analysis. An Elementar vario MICRO cube was used for elemental CHNS and O analysis. Powder X-ray diffraction (PXRD) was done on a PANalytical Xpert-PRO diffractometer (40 kV, 20 mA, $\lambda(Cu_{K\alpha1,\alpha2})$ = 1.541 Å, Bragg-Brentano mode, 2θ = 10 to 100°). Thermo Electron ESCALAB 250 spectrometer ($Al_{k\alpha}$ = 1486.6 eV, 15 kV, 6 mA) was used for the X-ray photoelectron spectroscopy (XPS) probing. Each survey spectrum has been collected at 1 eV per step (transition energy of 150 eV). Then, all high-resolution spectra have been recorded at 0.1 eV per step (transition energy of 20 eV). Photoelectron spectra were calibrated through the energy of the C=C component of the carbon C1s at 284.4 eV and appropriate charge compensation. The peaks fitting and the quantification were done on AVANTAGE software.

2.4. Electrochemical and catalytic measurements

General procedures. Cyclic voltammetry (CV), chronoamperometry (CA), and electrochemical impedance spectroscopy (EIS) were done on a SP-150 potentiostat (Biologic Science Instruments). A bipotentiostat-RRDE setup (AUTOLAB PGSTAT128N, Metrohm, Netherlands) was used to study ORR. The RRDE was 0.196 cm^2 glassy carbon disk (GC, 5 mm) and 0.072 cm^2 Pt ring. AUTOLAB PGSTAT204 potentiostat (Metrohm, Netherlands) was used for the characterization by EIS. Glycerol oxidation was studied on a RDE made of a 0.196 cm^2 GC. Ultrapure water (130 µL), isopropanol (50 µL), Nafion® suspension (20 µL), and 2000 µg of catalyst were ultrasonically mixed (water batch) to fabricate the ink of catalysts. Prior to the coating, the R(R)DE was mechanically polished by a slurry of alumina (particles size of 3, 1 and 0.05 µm). After washing with ultrapure water, it was cleaned by sonication for 5 min. Then, 4 µL were deposited onto the GC tip the (R)RDE (nominal loading of 40.7 μg_{Pd} cm^{-2} based on 20 wt.% theoretical), and rotator' speed was subsequently increased to 400 rpm and maintained till complete evaporation of the solvents under ambient conditions (5-10 min).[18] ORR (required several hours of operation) was studied at room temperature (23 ± 2 °C) in a custom-made polytetrafluoroethylene (PTFE) cell to resist alkalinity, and was cleaned by standard method.[28] Electrochemical studies were conducted in a basic three-electrode set up. Working, counter and reference electrodes were, respectively, a disk of GC (0.196 cm^2 covered with catalytic slurry), a plate GC (12.4 cm^2), and an Hg|HgO|(0.1 or 1 M) KOH reference electrode (MOE, RE-61AP, BAS Inc.). The potentials of the working electrode were then translated with regards to the RHE using the diagrams in Figure S1 and the formula $E_{RHE} = E_{MOE} + x$; x = 922, and 946 mV at 25 °C for KOH at 0.1, and 1 M, respectively.

CO stripping. The electrolyte was outgassed before the sequential cycling of electrodes (CV, 0.30-1.45 V_{RHE}) at 0.05 V s^{-1} (ten cycles), and 0.02 V s^{-1} (two cycles). After the

adsorption of CO at 300 mV_{RHE} (five minutes) and outgassing for 20 min, CV was run (0.02 V s^{-1}, three cycles).

Performance toward glycerol electrooxidation. The oxidation reaction of glycerol was assessed by the methods of CV, CA and EIS. The solution was outgassed with Ar. The potentiostatic EIS was implemented in the frequency scale from 100 kHz to 25 mHz at a fixed electrode potential (see the text), 10 mV amplitude, and 10 points per decade.

Electrolysis and high-performance chromatography (HPLC). Bulk electrolysis were realized in a bi-compartmentalized H-type cell separated by the hydroxide AEM. For the working electrode, both faces of a carbon paper (2×2 cm^2) were coated by the above catalytic ink at the same loading. A 16.5 cm^2 glassy carbon plate was the counter electrode. Electrolysis was done at 0.8 V_{RHE} for 2 h. The obtained reaction mixture was analyzed by HPLC (Dionex ICS-1000). Organic acids were separated by pKa strength with an UV−vis detector (λ = 210 nm) on a BP-OA Benson 2000-0 column (injecting of 25 μL, eluent = 25 mM H_2SO_4 at 0.4 mL min^{-1}). Assignments and quantifications were done through calibrations obtained by external standards expected from the glycerol oxidation.

ORR at RRDE. The collection efficiency (*N*) of the RRDE setup was evaluated in an outgassed 1 M KNO_3 electrolyte with $K_3[Fe(CN)_6]$ at a concentration of 0.005 M. *N* is the portion of the chemical species produced at the GC disk that effectively reach the Pt ring to react therewith. The assessed fraction of 0.245 ± 0.005 (Figure S2) is consistent within the company's specification of 0.249. ORR was studied by the methods of CV, LSV and accelerated stress test (AST: CV at 0.1 V s^{-1}, 0.6-1.0 V_{RHE}, 10000 cycles). The incomplete HO_2^- product of ORR (Eqs 1-2) in 0.1 M KOH (p*K*a(H_2O_2/HO_2^-) = 11.75) and the total transferred electrons per molecule of O_2 (n_{exp}) were evaluated online by Eqs. 3 and 4, respectively (see SI for details).[28-29] The kinetic current density j_k was evaluated by Eqs. 5-6,[28,30] termed to as "absolute activity". Then, j_k was converted into: (i) the active surface-area

specific activity (mA cm^{-2}_{metal}) by division of this value by the rugosity factor (cm^{2}_{metal} $cm^{-2}_{geometric}$), (ii) the weight activity (A mg_{metal}^{-1}) by division of this value by the precious metal content (μg_{metal} $cm^{-2}_{geometric}$).

Complete reduction: $O_2 + 2H_2O + 4e^- \rightarrow 4HO^-$, $E° = 1.23\ V_{RHE}$, (Eq. 1)

Incomplete reduction: $O_2 + H_2O + 2e^- \rightarrow HO_2^- + HO^-$, $E° = 0.76\ V_{RHE}$, (Eq. 2)

$$HO_2^-(\%) = \frac{200}{1 + \frac{N|I_D|}{I_R}} \quad \text{(Eq. 3)}$$

$$n_{ex} = \frac{4}{1 + \frac{I_R}{N|I_D|}} \quad \text{(Eq. 4)}$$

$$\frac{1}{j} = \frac{1}{j_{\lim}} + \frac{1}{j_k} \Rightarrow j_k = \frac{j \times j_{\lim}}{j_{\lim} - j} \quad \text{(Eq. 5)}$$

$$j_{\lim} = n_{ex} \times B \times \Omega^{\frac{1}{2}},\ B = 0.201 F C \upsilon^{-\frac{1}{6}} D^{\frac{2}{3}} \quad \text{(Eq. 6)}$$

I_D: current of the disk. I_R: current of the ring. j: current density of the disk. j_{lim}: current density of the plateau (O_2 mass transport limitation in electrolyte). n_{ex}: overall passed number of electrons per molecule of O_2. F(= 96485 C mol^{-1}): Faraday constant. D(= 1.9×10^{-5} cm^2 s^{-1} [31-32]): diffusion coefficient of O_2 in the electrolyte. Ω: speed of RRDE (rpm). C(= 1.2×10^{-6} mol cm^{-3}):[31-32] O_2 concentration in the electrolyte. ν(= 1.0×10^{-2} cm^2 s^{-1}):[31-32] kinematic viscosity of the electrolyte. j_k: mass-corrected kinetic current density (absolute activity).

2.5. Theoretical approach and computational details

Spin-polarized DFT calculations were performed using Perdew-Burke-Ernzerhof (PBE) formulation for the exchange-correlation energy functional,[33] as implemented in the Vienna Ab initio Simulation Package (VASP).[34] The electron-ion interactions were described by the Projector Augmented-Wave (PAW) method.[35-36] The electron wave functions were expanded

in a plane-wave basis set up to a kinetic energy cut-off of 400 eV. The positions of the atoms in the super cell were relaxed until the total energy differences fell below 104 eV. Pd(111) and PdFe(111) surfaces were calculated using slab models with a 3×3 surface unit cell, 5 layers (9 atom per plane) and a vacuum region of 15 Å. The two-bottom layer were frozen in the relaxed bulk positions, while the four topmost layers were allowed to relax. The Brillouin-zone integrations for flat surfaces were performed on a Monkhorst-Pack (331) k-point mesh. For the adsorption of glycerol, the gas molecule was adsorbed only on one side of the slab. As classic DFT cannot accurately capture weak interactions such as van der Waals forces, and it is always difficult to ascertain the existence of physisorbed states, DFT-D3 calculations including dispersion correction proposed by Grimme et al.[37] have been performed.

3. Results and discussion

3.1. Physicochemical characterization of supports

Before utilizing rGO and Vulcan XC72R carbon black supports to prepare Pd-based nanocatalysts, the textural properties of those carbon materials were evaluated by utilizing N_2 as the probing molecule.[38] Indeed, we first hypothesized that the thermal treatment of Vulcan will improve the surface properties. Figure 1a displays the N_2 isotherms of those substrates, synthesized (GO, rGO), pristine (Vulcan-p), and pretreated (Vulcan). Qualitatively, the hysteresis loop indicating the capillary condensation at higher pressure evidences the mesoporous character of the analyzed materials. The drastic difference between the GO-based materials and the Vulcan can be ascribed to the tremendous discrepancy in total pore volume (V_{tot}) and consequently available surface areas. Specifically, V_{total} = 0.011, 0.029, 0.461, and 0.623 $cm^3\ g^{-1}$ for GO, rGO, Vulcan-p, and Vulcan, respectively (Table 1). A deep analysis reveals that this volume is mainly composed of the mesoporous one in the case of Vulcan-p and Vulcan with $V_{meso}(cm^3\ g^{-1})$ = 0.307, and 0.514, respectively. The values are too

small for GO and rGO to enable a meaningful conclusion. Furthermore, the determined BET specific surface area confirms the above trend with $S_{BET}(m^2\ g^{-1})$ = 239.5 ± 1.5, and 413.9 ± 1.3 for Vulcan-p and Vulcan, respectively (Figure 1b). Those values correspond to 73% augmentation after the thermal treatment. A 23% improvement was reported for similar type of Vulcan carbon black ($S_{BET}(m^2\ g^{-1})$ = 262 (before), and 322 (after)), which was accompanied by a 2.2-fold boost in the electrochemically active surface area (ECSA) of platinum nanoparticles, and the improvement of the electrocatalytic activity in glucose oxidation.[27] It was argued that this enhancement results from the elimination of certain contaminants resulting from the production method and susceptible of obstructing some of the pores, sulfur being one of the presumed substances because its level in these types of carbonaceous matters may be higher than 1.3% by weight.[27,38] The determined mean pore size of 5-10 nm (Figure 1c, and Table 1) quantitatively confirms the mesoporous character (2-50 nm) of the materials. It is interesting to notice that the thermal treatment led to a 35% and 67 % increase of the total and mesoporous volumes, respectively.

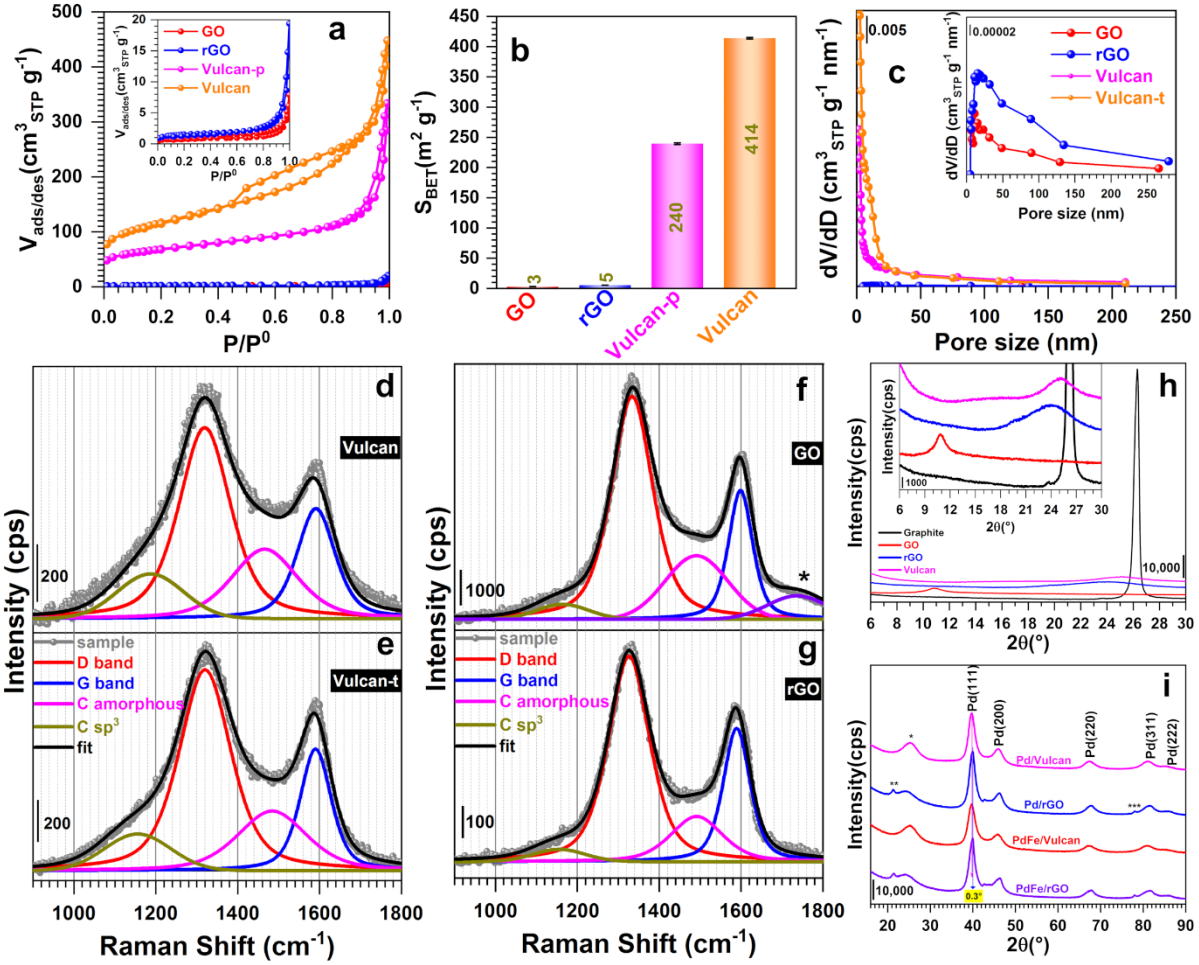

Figure 1. (a) Nitrogen isotherms. (b) S_{BET} for those carbon substrates. (c) Pore size (diameter) distribution. (d-g) Raman spectroscopy of: (d) Vulcan-p, (e) Vulcan", (f) GO, and (g) rGO. (h,i) PXRD of: (h) Graphite, GO, rGO and Vulcan (from bottom to up) without metal nanoparticles, and (i) rGO- and Vulcan-supported metal nanoparticles. "Vulcan" referred to as Vulcan XC72R carbon black and "p" referred to as pristine. Note: in panel (i), "*" indicates the presence of Vulcan XC72R while "**" and "***" indicate the presence of rGO.

To gain insightful information, we next performed the elemental analysis by CHNS, and O pyrolysis. The findings of Table 1 indicate that the sulfur content decreases from 0.83 to 0.72 wt.%. Meanwhile, the carbon decreases significantly from 97.84 to 91.36 wt.% while oxygen content augments from 1.47 to 7.04 wt.%. Those unexpected results indicated that the

presence of significant oxygenated functions within the carbon structure (of high importance for getting an optimal wettability or hydrophobic/hydrophilic character) will be beneficial for nanoparticles deposition and/or obtaining high electrocatalysis in aqueous media.

We next aimed to identify the type of carbon matters that are present in/on those substrates through the determination of the length of graphitization L_a (Eq. 7), the quantification of defects, and the size of in-plane crystallites. To this end, Raman spectroscopy experiments were performed and the obtained Raman spectra were decomposed using pseudo-band Voigt functions. Figures 1d-g show that the analyzed materials exhibit the same profiles, in agreement with previous reports.[25,27,39-40] Table 1 outlines the data of interest. The graphitic G-band (G-mode, E_{2g} symmetry) is characterized by the peak at 1590 cm^{-1} (C=C stretching, sp^2-bonded C in-plane vibration, area A_G). In the other side, the band situated at 1320-1330 cm^{-1} is named D-band (or D-mode, A_{1g} symmetry, area A_D), is typical of the symmetry breakdown for edge C of sheets and growth when the number of defects increases in graphene lattices.[25,27,38-39] The obtained values of A_D/A_G = 2.9 (GO), 2.3 (rGO), 2.3 (Vulcan-p), and 2.7 (Vulcan) indicate a slight change of the graphitization upon the reduction of GO or the thermal treatment of Vulcan. Correspondingly, the deduced value of L_a(nm) = 15.5 (GO), 19.4 (rGO), 19.4 (Vulcan-p), and 16.8 (Vulcan) shows a modification, which suggests that the long-distance order sp^2 group size was adversely impacted by the reduction of GO or by the heat treatment of Vulcan-p.[39]

$$L_a(nm) = \left(2.4\times10^{-10}\right)\lambda^4\left(\frac{A_D}{A_G}\right)^{-1} \qquad \text{(Eq. 7)}$$

λ(nm): wavelength of the used laser. A_D: area of the band D. A_G: area of the band G.

Table 1. Physicochemical properties: N_2 adsorption-desorption, Raman Spectroscopy, and CHNSO. n.d. = not determined. "Vulcan" = Vulcan XC72R carbon black and "p" = pristine.

Entry		GO	rGO	Vulcan-p	Vulcan
N_2 adsorption-desorption	$S_{BET}(m^2\ g^{-1})$	2.9	5.4	239.5	413.9
	$R_{BHJ}(nm)$	4.1	5.0	2.5	2.5
	$V_{total}(cm^3\ g^{-1})$	0.011	0.029	0.461	0.623
	$V_{microporous}(cm^3\ g^{-1})$	0.005	0.016	0.154	0.109
	$V_{mesoporous}(cm^3\ g^{-1})$	0.006	0.013	0.307	0.514
Raman spectroscopy	$\nu_D(cm^{-1})$	1333	1326	1320	1320
	$\nu_G(cm^{-1})$	1598	1589	1591	1590
	A_D/A_G	2.9	2.3	2.3	2.7
	$L_a(nm)$	15.5	19.4	19.4	16.8
CHNS	C(wt%)	n.d.	n.d.	97.84 ± 0.18	91.36 ± 0.29
	H(wt%)	n.d.	n.d.	0.36 ± 0.11	0.50 ± 0.01
	N(wt%)	n.d.	n.d.	0.06 ± 0.05	0.07 ± 0.01
	S(wt%)	n.d.	n.d.	0.83 ± 0.06	0.72 ± 0.03
O pyrolysis	O(wt%)	n.d.	n.d.	1.47 ± 0.02	7.04 ± 0.04

Furthermore, we undertook PXRD measurements to determine the crystal structure of the supports (rGO and Vulcan) and the supported materials. In order to provide a fair analysis of the rGO sample, the parent composites of GO and graphite were run as controls. The recorded PXRD patterns of the supports are displayed in Figure 1h. The initial graphite has a strong peak at 2θ = 26.6° attributed to scattering by the (002) crystallographic planes.[26,40-41] Vulcan carbon black shows a broad feature at 25.2° deriving from reflections on less-organized stacked carbon planes.[27] The complete disappearance of the peak at 26.6° and the emergence of a peak at 10.9° confirm the successful synthesis of GO.[26,40-41] Furthermore, according to previous reports, the absence of the latter peak and the presence of the broad peak situated at 24.0° suggest that rGO is well organized with 2D sheets and that the surface functional units were effectively eliminated.[40-41] Figure S3a shows the high-resolution PXRD

of GO, and rGO. The additional peaks at 42.7° and 78.0° (also visible in Figure 1i) are related to the crystalline structure of carbon atoms in the graphene plane, respectively indexed as (100) and (110). The results from the peak width calculation show that the starting graphite is made of a 20 nm stack of 60 layers of graphene sheets. For the GO derived from it, the stacking ranges over 6 nm, i.e. 8 planes. By XRD calculation, the fabricated rGO is of 1.5 nm thick, i.e. 4 sheets. However, given the low BET surface of GO-based materials compared to other reported systems (tens to hundreds of m^2/g),[41] the later data by XRD are underestimated because we observed on several TEM images (Figure S4) that the thickness is not so homogeneous leading to a much higher number of layers on some parts.[39] Having physicochemically characterized the two supports of rGO and Vulcan, we next sought to get in a first attempt, the crystallinity and crystallographic structure of the as-synthesized four types of nanomaterials Pd/Vulcan, PdFe/Vulcan, Pd/rGO, and PdFe/rGO. The results are shown in Figure 1i. For Vulcan-supported nanomaterials, the diffraction peak deriving from the (002) planes of graphite at 25.3° is almost found at the same position as in the absence of the metallic nanoparticles. However, the data of rGO-supported materials highlight the presence a second diffraction peak at 21.2° in addition to the initial peak of rGO localized at 24.0° (plus those discussed above at 42.7° and 78.0°). Similar shift of the position of the diffraction peak (thus the *d*-spacing) was observed when rGO was prepared under different chemical conditions and attributed to the degree of the reduction that affects the ordering of the two-dimensional sheets of rGO.[40] The present findings would indicate that the chemical reduction of the palladium (II) precursor by the $NaBH_4$ and the subsequent deposition of the metallic nanoparticles strongly affect the ordering of the two-dimensional sheets of rGO. The second explanation is that this peak was already present in the rGO, but it was masked by the broader peak at 24° (Figure S3b). In fact, there would be 2 types of rGO, a minority made of nanosheets with a larger interplanar distance (giving a peak at 21°), and a dominant phase

composed of less-organized (oriented) nanosheets of narrower inter-sheet distance showing a peak at 24° (similar to Vulcan). After the nanoparticles deposition, the texture of the rGO species in the Pd(Fe)/rGO materials dramatically changes and results in a better orientation of the widely spaced sheets, whose signal appears to be much higher.

On the other hand, it can be qualitatively observed that unlike previous report of PdFe/C nanocatalysts,[42] no isolated Fe or FeO_x particles are present on the diffraction patterns. This would suggest the formation of a single PdFe phase (alloy). In fact, for both Pd/Vulcan and PdFe/Vulcan materials, (111), (200), (220), (311), and (222) planes of palladium (fcc symmetry) are situated at 39.7°, 46.0°, 67.4°, and 81.2°, respectively. For Pd/rGO and PdFe/rGO, the peaks are situated at the same positions and the latter shift toward higher 2θ by 0.3°. The determined crystallite size by Scherrer's law is of about 4 nm for PdFe/Vulcan and 5 nm for others (i.e. Pd/Vulcan, Pd/rGO, PdFe/rGO). The first observation means that there was no *a priori* significant distortion of the initial crystal structure of Pd upon incorporation of Fe to form PdFe nanoalloy that was expected to have higher angles relative to Pd.[3,43-44] The results from the quantitative analysis by ICP-OES confirmed the theoretical targets of about 20 wt.% metal loading and $Pd_{0.8}Fe_{0.2}$ as the bulk atomic composition. Indeed, the Pd content is about 19.5 wt.% in monometallic and 17 wt.% in bimetallic where Fe content is 2 wt.%, i.e., $Pd_{0.82}Fe_{0.17}$ atomic compositions. Their lattice parameters being a(Pd) = 3.89 Å and a(Fe) = 2.86 Å, the introduction of about 20 at.% of Fe was expected to be accompanied by a change of the lattice parameter of Pd and hence the shift of the diffraction peaks.[3] Furthermore, a strong support-metal interaction could explain the peak decoupling (rGO) at 2θ = 21.2° and 24.0° as well as the noticed encapsulation of the nanoparticles between the graphene sheets in Figure S4. These findings would foreword a significant improvement in electrocatalytic properties.

3.2. TEM, STEM-EDX, and XPS characterization of the synthesized electrocatalysts

To obtain in-depth knowledge about the size of nanoparticles, compositional features of bimetallic materials, and surface state of nanocatalysts, we next performed deeper analysis by TEM, STEM-EDX, and XPS. Figures 2a-h show the TEM images. Extended TEM micrographs of rGO-supported Pd and PdFe particles in Figure S4 highlight the layered structure of rGO as well as the embedding of the nanoparticles between the graphene sheets. The particles size is 2-10 nm for Pd/Vulcan and PdFe/Vulcan materials. For Pd/rGO and PdFe/rGO materials, very small nanoparticles (2-10 nm) coexist with large size nanoparticles (15-30 nm). This disparity could be explained by the nature of the support because, in contrast to Vulcan, the surface composition of rGO is not fully homogeneous,[39] which alters the seeds nucleation/growth into particles. HRTEM pictures (Figures 2i-j, and Figures S5-7) show an interplanar space of 0.23 ± 0.1 nm, which indicates the presence of the (111) crystalline plane of fcc Pd.

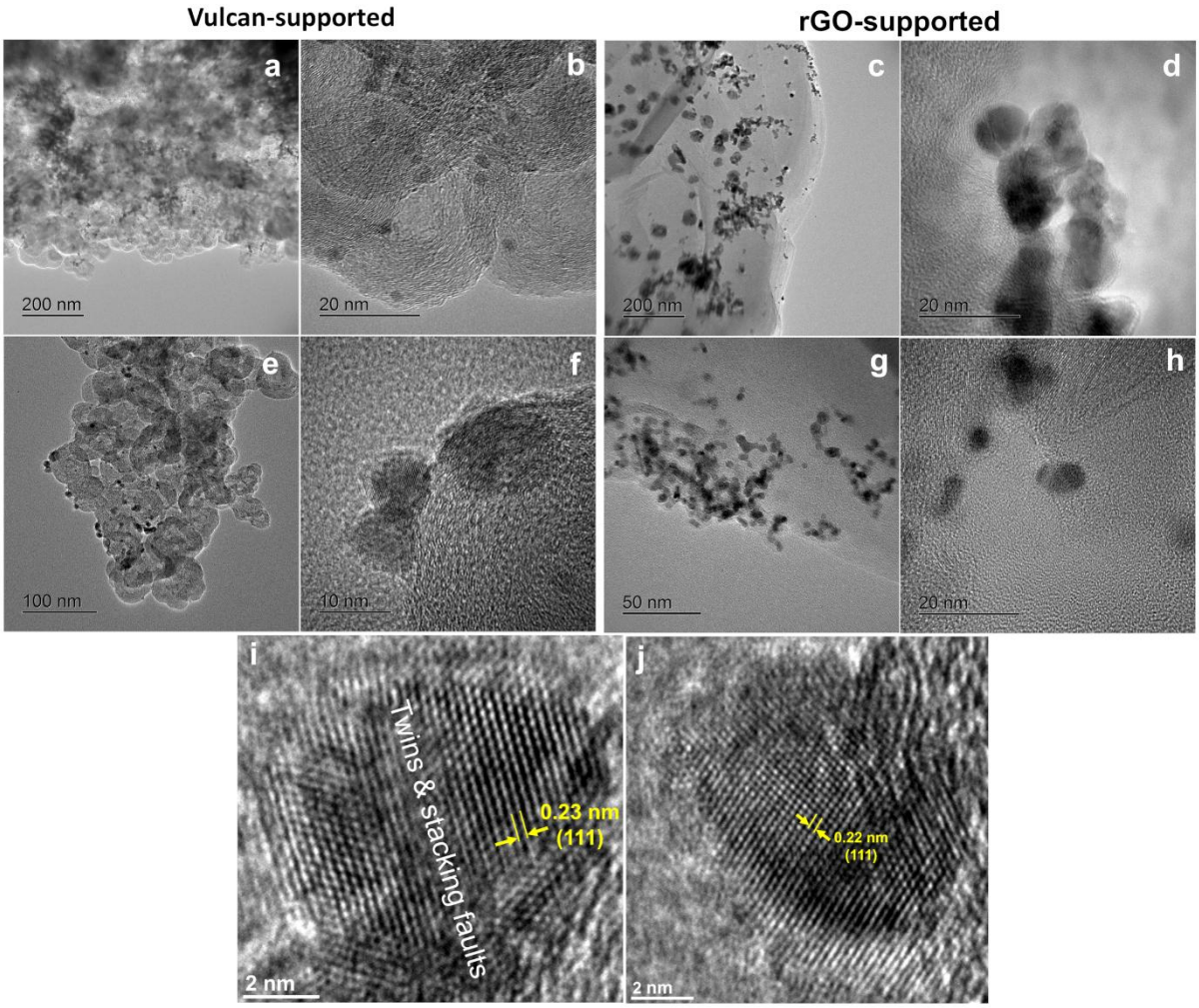

Figure 2. (a-h) TEM micrographs of Vulcan-supported, and rGO-supported nanoparticles: (a, b) Pd/Vulcan, (c, d) Pd/rGO, (e, f) PdFe/Vulcan, and (g, h) PdFe/rGO. (i-j) HRTEM of PdFe.

We next utilized the STEM-EDX analysis to precisely localize the position of Pd and Fe for unraveling the exact structure of the nanostructured PdFe. Figures 3a-c show the individual and overlay EDX mapping of PdFe/Vulcan. Extended results of TEM, STEM, and EDX line profiles are reported in Figures S8a-g. These results indicate a surface enrichment by Fe for the bimetallic nanostructures. Quantitatively, a single nanoparticle of PdFe/Vulcan is composed of 85 at.% Pd and 15 at.% Fe (Figures 3c, and S8b). For a set of nanoparticles (Figure S8a), the composition is 81 at.% Pd and 19 at.% Fe. These data confirm the theoretical target of $Pd_{0.8}Fe_{0.2}$, previously attested by the bulk ICP-OES analysis. Given the

two types of particles size for PdFe/rGO, we performed the maps for a larger particle (Figures 3d-f), and a smaller one (Figures 3g-i) in an attempt to provide a sound representation of the sample.

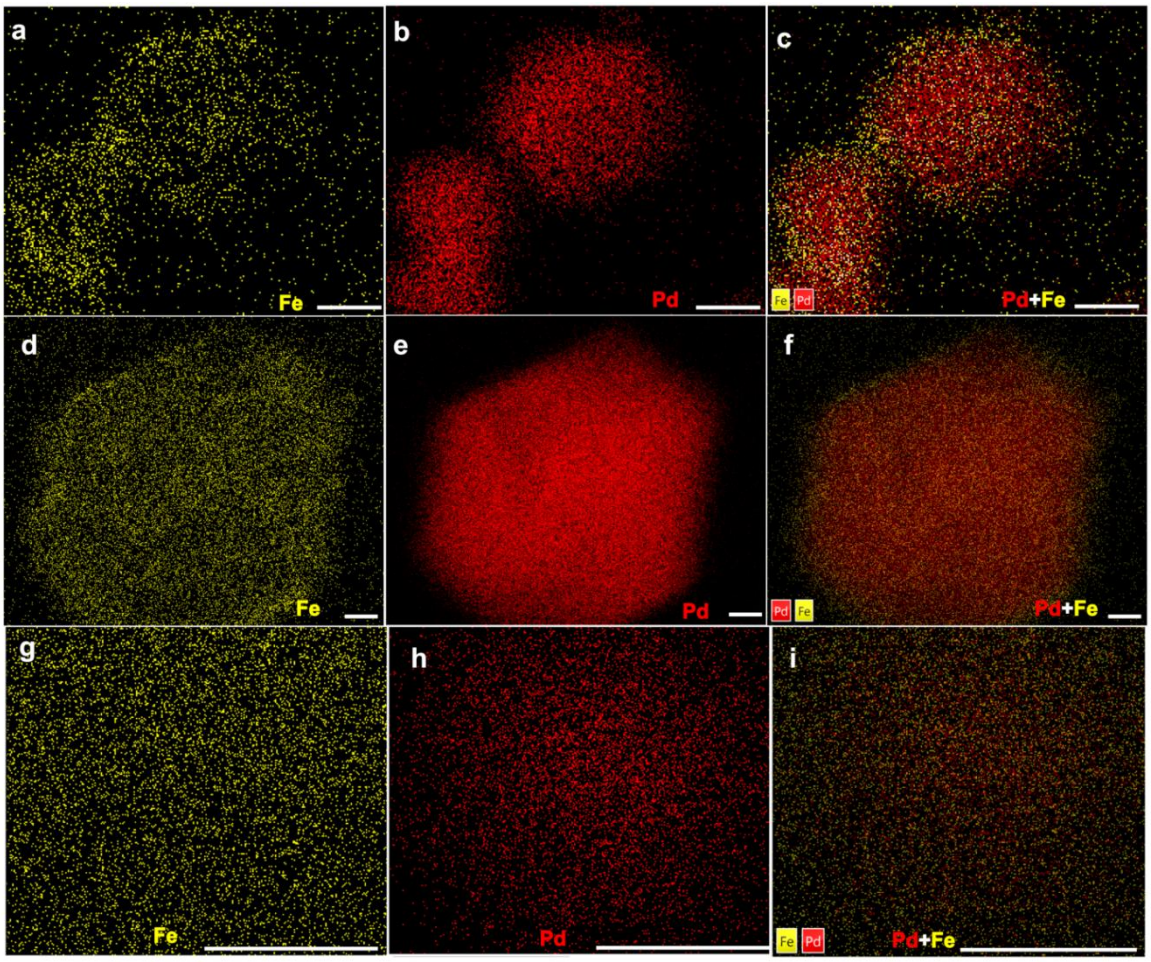

Figure 3. STEM-EDX images of: (a-c) PdFe/Vulcan, (d-i) PdFe/rGO. Elemental mapping of Fe, Pd, and Fe+Pd. Scale bar = 5 nm.

A closed look at the pictures indicates a surface enrichment by Fe for nanoparticles of a large size. For small nanoparticles, Fe signal looks more homogeneous (Figure 3g) while the palladium signal is stronger within the center of the particle (Figure 3h), like the situation of PdFe/Vulcan (Figure 3a *versus* Figure 3b). For bigger particles, the composition is about 90 at.% Pd and 10 at.% Fe while in smaller particles, the trend is about 70 at.% Pd and 30 at.% Fe. These imaging results clearly explain why there was no additional diffraction peak for the

bimetallic materials because Pd and Fe are all together in the same nanoparticle. Even though a nanoalloy structure with a strong change of the lattice parameter was not formed, an improvement of the electrocatalytic properties cannot be, however, excluded because the alloy strategy is only one of the multiple ways of tuning the efficiency of a bimetallic catalyst; core-shell/skin approaches being some of them.[9,45-48]

We finally utilized the physicochemical method of XPS to interrogate the surface properties of the prepared nanocatalysts. The survey XPS spectra are reported in Figure S9. The high-resolution spectra of Pd 3d and Fe 2p are displayed in Figures 4a-d, and Figure 4e, respectively. Doublets result from the splitting of the spin-orbit system ($j = l \pm ½$, $l = 1$ (*p*), and 2 (*d*)). The binding energy (BE) of the Pd $3d_{5/2}$ component of metallic palladium[49-50] is BE = 335.1, 335.1, 335.2, and 335.2 eV for Pd/Vulcan, Pd/rGO, PdFe/Vulcan, and PdFe/rGO, respectively. Even if it is within the measurement error, a slight shift of the energy level of 0.1 eV reflecting a change in the electronic environment of Pd can be observed. For Pd $3d_{3/2}$ of PdO,[49-50] BE = 336.0 eV (Pd/Vulcan), 336.0 eV (Pd/rGO), 335.9 eV (PdFe/Vulcan), and 336.0 eV (PdFe/rGO). According to the literature,[49-50] the peak at BE = 337.3 eV (Pd/Vulcan), 337.5 eV (Pd/rGO), 337.5 eV (PdFe/Vulcan), and 337.4 eV (PdFe/rGO) belongs to superior oxides of PdO_x ($x > 1$). The extracted quantitative data (Figure 4f) of the identified species of Pd metal, PdO, and PdO_x ($x > 1$) reveal that rGO-supported nanomaterials have the highest amount of surface Pd metal of ca. 70 at.%. The slight decrease of metallic Pd in bimetallic compositions in comparison to the monometallic could result from the palladium atoms involved in electronic interaction with iron that weakens the Pd-Pd bound. This modulation of the Pd-Pd bound is expected to exalt the catalytic activity.[3,51-52] From Figure 4e, the peaks at 711.0, and 724.7 eV belong, respectively, to Fe $2p_{3/2}$, and Fe $2p_{1/2}$ of di- and/or trivalent iron atoms.[43,53] Indeed, seminal XPS investigations of either iron or palladium-iron materials have shown that iron exposure to

humidity leads to a multilayered hydroxyl/oxide matter.[53] Basically, when a metal (particularly a transition metal or non-noble metal) is subjected to the atmospheric air, it naturally begins a complex chemical oxidizing process, whereby the formation a passivation film shields the material from profound oxidation. This natural reaction can also explain the presence of oxidized species of palladium. This is particularly true because high-resolution PXRD (Figure 1i) did not detect any Pd oxide. Besides, a direct correlation between the XPS results of iron and the above findings from STEM-EDX is obvious because, at this stage, iron at the surface of nanostructure exposes the entire Fe atoms to this natural surface oxidation.

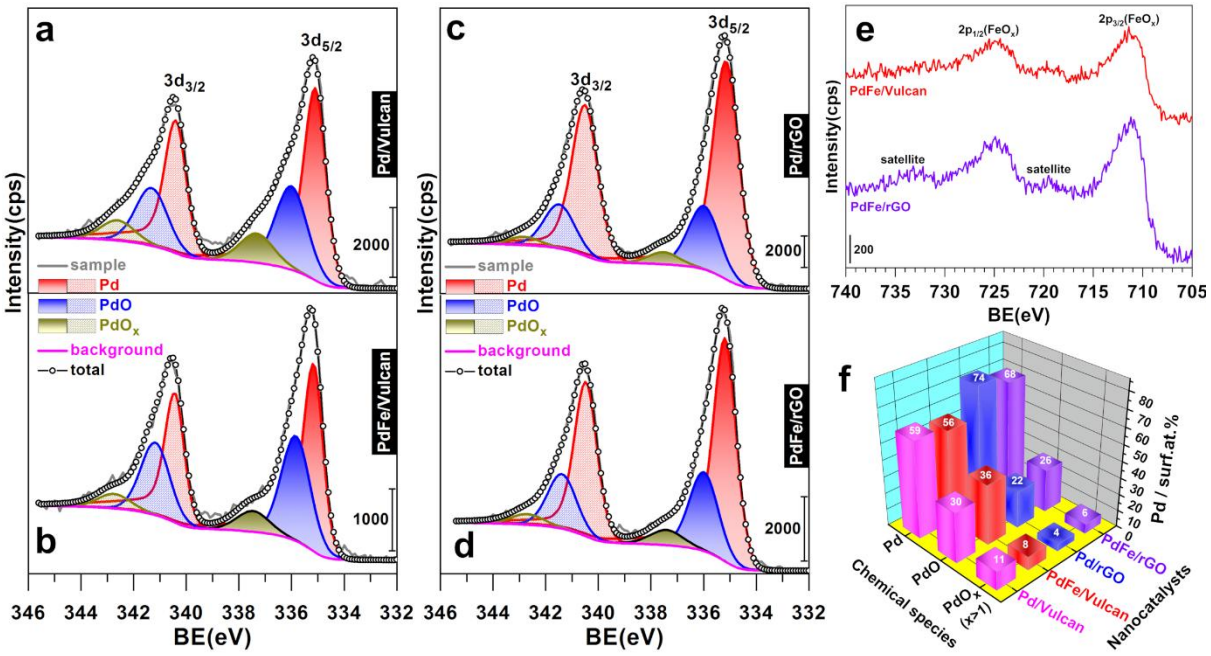

Figure 4. XPS characterization. (a-d) Decomposed spectra of Pd 3d: (a) Pd/Vulcan, (b) PdFe/Vulcan, (c) Pd/rGO, and (d) PdFe/rGO. (e) High-resolution spectra of Fe 2p region. (f) Overall quantitative data from panels (a-d).

3.3. Electrocatalytic performance towards CO and glycerol oxidation reactions

The previous characterizations have demonstrated our ability to use either the support or iron to change the physicochemical characteristics of Pd-based nanomaterials. We next electrochemically and electrocatalytically interrogated the ability of those materials to

efficiently perform the glycerol oxidation in an alkaline environment. Before that, we preliminarily utilized CO as the smallest organic and probe molecule to examine the catalytic properties. In order to provide a fair comparison under our experimental conditions, we used commercial nanocatalyst Pd/C (20 wt.%) at similar metal loading (ca. 40 μg_{Pd} $cm^{-2}_{geometric}$). This will enable an immediate confrontation of the electrochemical behaviors before comparison with the existing data in the literature. It should be clarified that given the considered potential target of 300-1450 mV_{RHE}, iron does not have a significant activity toward both CO and glycerol electrooxidation. Thus, in the followings, any improved electrocatalytic kinetics of PdFe relative to Pd will be the result of the induced synergistic effect in the bimetallic. Figure 5a displays the recorded CV profiles for the different electrodes. The current was normalized to ECSA of palladium that was evaluated by the method of its oxide reduction peak, as explained in ref.[54]. Figure 5b displays the different regions. The OH^- adsorption onto metallic palladium to form $Pd(OH)_x$, and the beginning of the adsorbed CO oxidation are characterized by the region A1. The complete oxidation of the adsorbed CO is marked by the peak A2. The evolution of $Pd(OH)_x$ into PdO occurs in the region B, and the reduction of the formed PdO into Pd produces the peak C. The comparative voltammograms are shown in Figure 5c and additional plots versus the electrode area (geometric) and/or the palladium content are reported in Figure S10a-d. The good start of the oxidation on bimetallic electrodes at low potentials is confirmed by the position of the peaks which shift negatively, a proof of an enhancement of the electrochemical kinetics. Specifically, the position of the peak current density decreases in the order Pd/C (843 mV_{RHE}) > Pd/Vulcan (802 mV_{RHE}) > Pd/rGO (792 mV_{RHE}) > PdFe/rGO (778 mV_{RHE}) > PdFe/Vulcan (772 mV_{RHE}). It is noteworthy that the iR-drop impact on this trend is negligible because of the range of the currents and the determined ohmic resistance, which is similar for all electrodes (see below). These findings comfort our hypothesis that the aforementioned

modification of the physicochemical characteristics of Pd by either the support or iron positively accelerates the electrocatalytic kinetics.

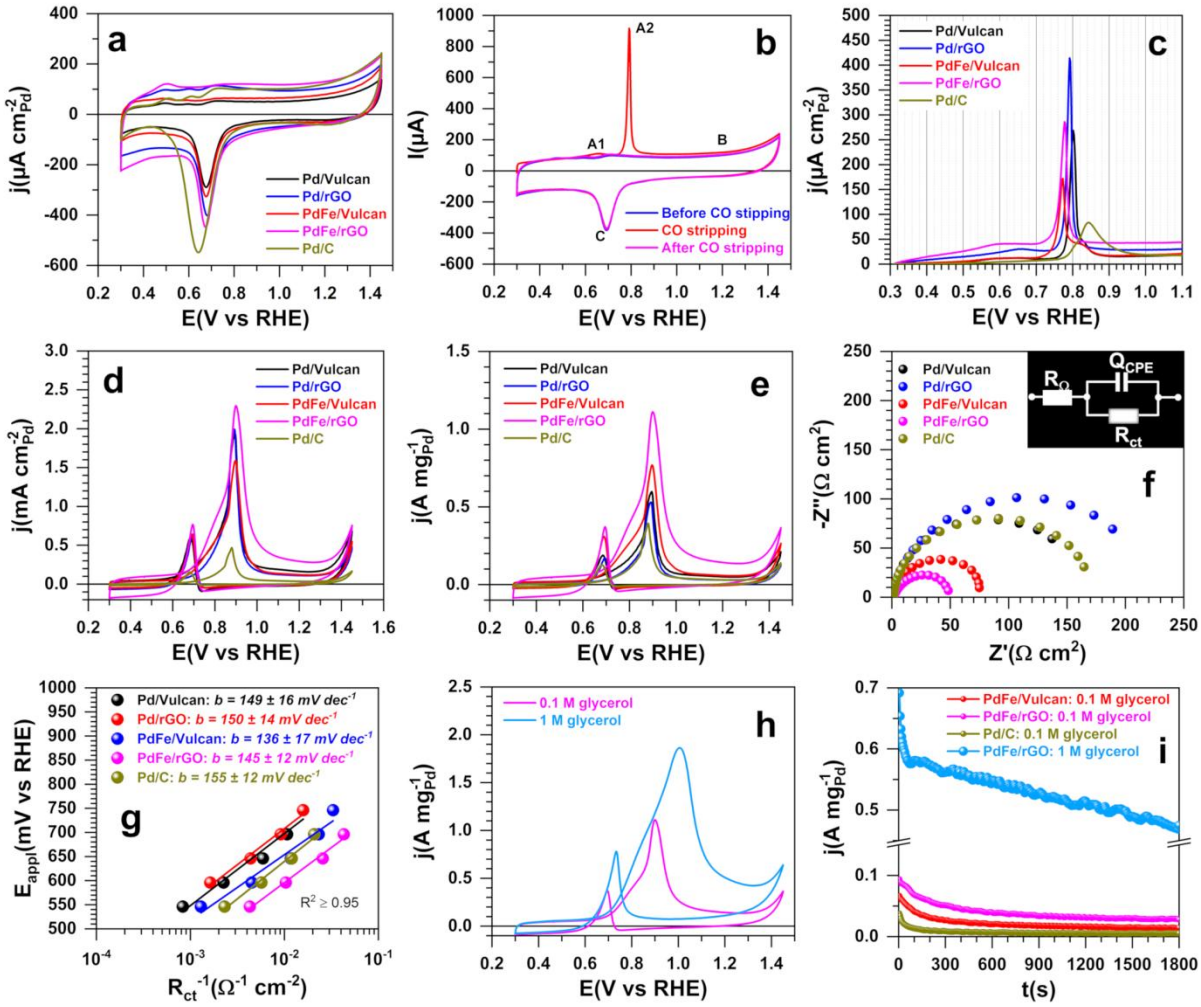

Figure 5. Comparative performance of the benchmark catalyst Pd/C, and those prepared for CO stripping and glycerol electrooxidation (1 M KOH, 25 °C). (a) Blank CVs (0.05 V s^{-1}) related to the specific active surface of Pd. (b) Typical CVs (0.02 V s^{-1}) recorded during a CO stripping experiment for the synthesized Pd/rGO material. (c) CVs (0.02 V s^{-1}) of CO stripping by ECSA of Pd. (d) CVs (0.05 V s^{-1}) of glycerol oxidation by Pd weight. (e) CVs (0.05 V s^{-1}) of glycerol oxidation by ECSA of Pd. (f) EIS of glycerol oxidation at 0.646 V_{RHE}: Inset the EEC of $R_{\square}$ + Q_{CPE}//R_{ct}. (g) R_{ct}-based Tafel plots. (h) CVs (0.05 V s^{-1}) in the presence of glycerol on PdFe/rGO electrode by palladium weight. (i) CA at 0.85 V_{RHE} (un-

stirred solution). Glycerol concentration was 0.1 M for panels (d-g). The potentials were iR-drop uncorrected.

Table 2 gathers the evaluated ECSA that was used to assess the CO coverage of $ECSA_{CO}/ECSA_{PdO}$ = 0.76 (Pd/Vulcan), 0.86 (Pd/rGO), 0.64 (PdFe/Vulcan), 0.75 (PdFe/rGO), and 0.77 (Pd/C). These values are in the range of the maximum CO coverage of 0.68-0.79 because of the combination of linear and bridge adsorption of CO on metallic surfaces.[55] Furthermore, despite its high ECSA, the commercial Pd/C does not provide the highest current density regardless of the type of normalization (Figures 5c, S7b, and S7d). The bimetallic compositions have a lower peak current density simply because of the reduced CO coverage and the electrooxidation of a single (and fixed at the surface) layer of CO. For the electrooxidation of a compound in the bulk solution such as glycerol, the conclusion is often different. Conclusively, these first electrocatalytic studies clearly highlighted how the present electrocatalysts are superiors to the standard material.

Table 2. Performance metrics (25 °C, [KOH] = 1 M) of Pd/C (commercial) and as-prepared catalysts. CO stripping and glycerol electrooxidation. EIS at 646 mV_{RHE}.

Entry	CO stripping				Glycerol (0.1 M) electrocatalysis			
	$ECSA_{PdO}(m^2 g^{-1})$	$ECSA_{CO}(m^2 g^{-1})$	$ECSA_{CO}/ECSA_{PdO}$	$E_p(mV_{RHE})$	$E_{onset}(V_{RHE})$	$j_p(mA\ cm^{-2}{}_{Pd})$	$j_p(A\ mg^{-1}{}_{Pd})$	$R_{ct}(\Omega\ cm^2)$
Pd/Vulcan	31	24	0.76	802	0.52	1.94	0.60	169.3
Pd/rGO	27	23	0.86	792	0.52	1.99	0.53	228.5
PdFe/Vulcan	38	24	0.64	772	0.52	1.59	0.77	85.4
PdFe/rGO	38	28	0.75	778	0.52	2.30	1.11	96.4
Pd/C	102	79	0.77	843	0.58	0.47	0.39	175.4

Having shown that both the iron and the support improve the electrocatalysis of Pd nanoparticles towards the adsorbed CO, we next explored the reactivity of glycerol at these catalytic surfaces. Figures 5d-e show the recorded CVs when normalized by either the ECSA or the mass of Pd. Extended, and control data are reported in Figures S11-S15. The shape of the curves with two oxidative peaks is typically characteristic of an alcohol electrooxidation reaction at metallic catalyst. During the forward sweep of the potential, the glycerol adsorption at metallic and/or hydroxylated palladium surface followed by the subsequent oxidation of glycerol produces a peak current around 0.89 V_{RHE}. For higher potentials, the surface begins to become covered with oxides that are electrocatalytically inactive, but their reduction during the backward scan releases new metallic active sites that will produce a new peak current (Figure 5d *versus* Figure 5a).

EIS was also utilized to provide a deeper understanding of the electrocatalytic performance for the tested nanostructures in the kinetic region, i.e., low potential range of 546-746 mV_{RHE}. Figure 5f shows the comparative results by the complex-plane Nyquist impedance. Extended data are reported in Figures S14a-f. The data were fitted (see Figure S15) by the representative equivalent electrical circuit (EEC) of R_Ω+Q_{CPE}//R_{ct} (inset of Figures 5f, and S14f), which best describes the investigated electrocatalytic interface. Table S1 gathers the fitted data of the charge transfer resistance R_{ct} (electrochemical kinetics), the uncompensated resistance R_Ω (ohmic loss), and the constant phase element Q_{CPE} (double-layer).[56] As resumed in Table 2, R_{ct} at 646 mV_{RHE} follows the trend Pd/rGO (228.5 Ω cm^2) > Pd/C (175.4 Ω cm^2) > Pd/Vulcan (169.3 Ω cm^2) > PdFe/rGO (96.4 Ω cm^2) > PdFe/Vulcan (85.4 Ω cm^2). Given that R_{ct} ≈1/$k°$ (standard rate constant), and ≈1/j_0 (exchange current density), these results clearly highlight the substantial enhancement of the electrochemical kinetics of the bimetallic materials. Specifically, an enhancement factor of ca. 2 is observed for PdFe/Vulcan compared to commercial Pd/C. The Tafel slopes in Figure 5g confirm the excellent ability of

PdFe/Vulcan for fast electron transfer in the potential range of 546-746 mV_{RHE}. In the mixed region of 720-850 mV_{RHE} (before mass transport limitation around 0.89 V_{RHE}), the bimetallic catalysts showed an enhanced oxidation behavior. Quantitative data of the peak current density of j_p = 1.59-2.30 mA cm^{-2}_{Pd} (or 0.53-1.11 A mg^{-1}_{Pd}) support the high activity of the home-made materials over the commercial Pd/C for which j_p = 0.47 mA cm^{-2}_{Pd} (or 0.39 A mg^{-1}_{Pd}). Especially, those specific and mass activity metrics of PdFe/rGO were found to be 4.9, and 2.8 fold larger than Pd/C, respectively. Figure S11a also shows the best up activity of PdFe/rGO with j_p = 35, and 59 mA $cm^{-2}_{geometric}$ for 0.1, and 1 M of glycerol, respectively. Literature-based performance indicators of pertinent metal nanocatalysts for the glycerol electrooxidation in basic electrolytes are gathered in Table S2, wherein j_p = 20-290 mA cm^{-2}_{geo} (0.2-18 A mg^{-1}_{metal}) and where the metal loading can be very high, i.e. reaches 500 μg_{metal} cm^{-2}.[6,8-12,45] Furthermore, at 1 M glycerol (Figures 5h, S8b, and S8c), the achieved j_p = 4 mA cm^{-2}_{Pd} (2 A mg^{-1}_{Pd} and 59 mA cm^{-2}_{geo}) on the PdFe/rGO electrode is higher than the reported 3 mA cm^{-2}_{Pd} (1 A mg^{-1}_{Pd} and 12 mA cm^{-2}_{geo}) for PtCo nanocubes.[10] The chronoamperometry experiments in Figure 5i substantiate the good stability of the developed nanocatalysts. It can therefore be briefly summed up that not only a clear increase in electrocatalytic performance compared to the commercial/standard material has been achieved for the home-made materials, but also high current densities were recorded relative to most of the nanocatalysts in the literature.

We finally collected CVs at different scan rates (v) to study the glycerol oxidation process electrochemically. The results show that when v increases, j_p also augments (Figures S11d, and S12). The log-log scale plots of j_p versus v represent straight lines with a slope of 0.23-0.27 (Figure S13). Basically, a slope of 1 means that the adsorption is the limiting process while a slope of 0.5 indicates a limitation by the diffusion (when both prevail, the slope is 0.5-1), and a slope lower than 0.5 suggests complex processes as well as the electron

transfer.[57] In the present case, it can be concluded that the improvement of the performance relies on a command over the phenomena of the reactant(s) adsorption, reactant(s)/product(s) diffusion, and electron transfer. This is not surprising as the electrooxidation of glycerol is a coupled proton and electron transfer processes.

3.5. Electrocatalytic performance towards oxygen reduction reaction (ORR)

Having demonstrated that the prepared bimetallic compositions can be excellent candidates for the electrocatalytic oxidation of glycerol, we sought to study more carefully whether those materials can also be suitable for ORR. The motivation was to produce a multifunctional (roughly referred to as bifunctional) material working as anode and cathode (not at the same electrode). We evaluated the efficiency by integrating the common long-term electrochemical stability protocol.[14-16,22] It was an accelerated potential cycling program at 0.1 V s^{-1} (0.6-1.0 V_{RHE}) in O_2-saturated electrolyte for 10000 cycles (1 cycle = forward + backward), hereafter termed as AST (accelerated stress test). As expressly outlined in Introduction, we also aimed to question whether the evaluation of the kinetic parameters for this reaction in alkaline media at Pd-based nanomaterials depends greatly on how the polarization curves were recorded or not. Figures 6a-f clearly underscore the strong influence of the direction of the potential scanning on the performance of ORR. The extracted data of interest, i.e., E_{onset}, $E_{1/2}$, and j_k are gathered in Tables S3-S4. The best values of these indicators were obtained when the electrode potential was swept in the anodic sense, i.e., from low to high potential. The latter was set at the open circuit potential OCP, i.e., the current at zero current $E_{I=0}$ (theoretical equilibrium potential of the redox couple O_2/HO^- if 100% faradaic efficiency) to avoid modifying strongly the metallic surface. The augmentation of $\Delta E_{onset,a/c}$ = 20 mV is accompanied by an increase of $\Delta E_{1/2,a/c}$ = 30 mV for Pd/C, by switching from cathodic to anodic direction. The change of the kinetic current density is $j_{k,a}/j_{k,c}$ = 3.4, 5.9, 5.2, and 4.2 at

0.95, 0.90, 0.87, and 0.85 V_{RHE}, respectively. For the same potential trend at PdFe/rGO electrode, our findings indicated that $\Delta E_{onset,a/c}$ = 20 mV and $\Delta E_{1/2,a/c}$ = 60 mV while $j_{k,a}/j_{k,c}$ = 19.0, 6.9, 3.4, and 2.4, respectively. As reported in Figures S16-S17, the amount of the indirect product of hydroperoxide anion HO_2^- and transferred number of electrons (n_{ex}) do not change significantly. Combined with earlier findings at Pt catalysts in acidic media,[18] the present results at Pd-based electrocatalysts in a basic electrolyte definitely underpin the conclusion that, the oxide of Pt or Pd surface inhibits the ORR kinetics.[18] The anodic direction was further chosen.

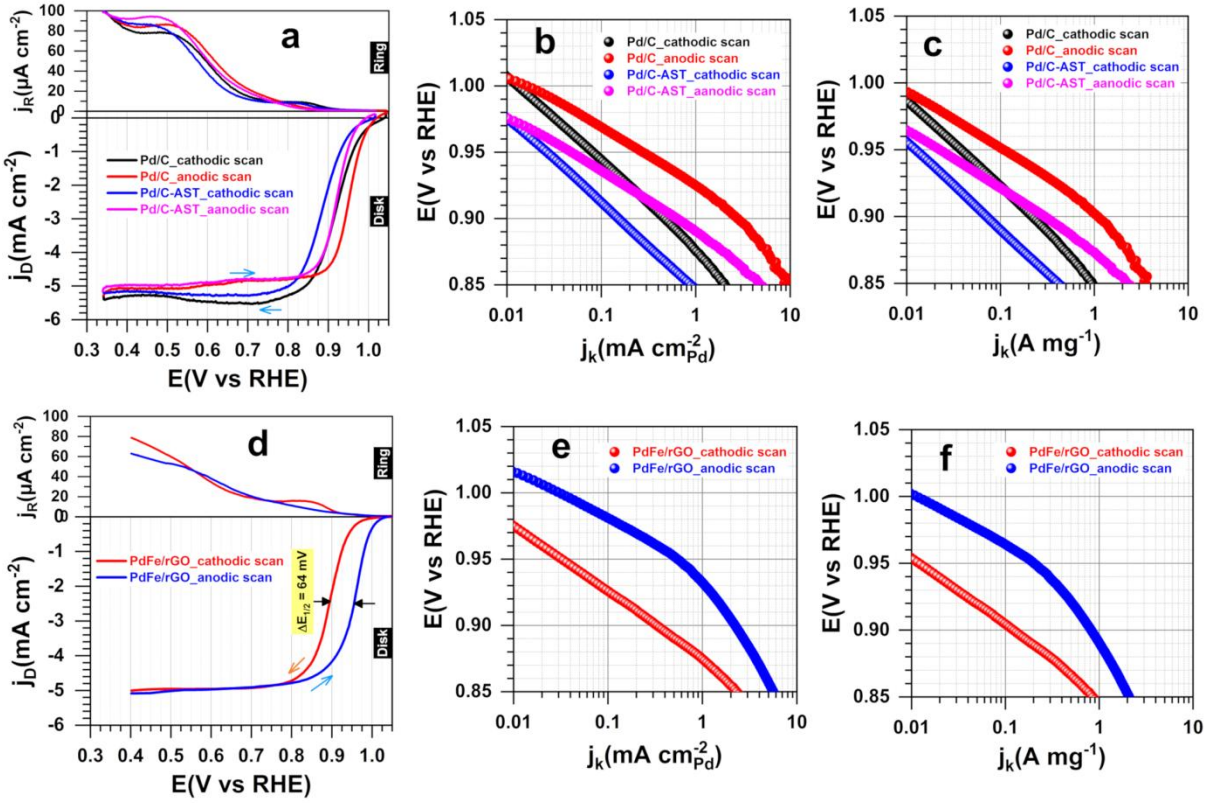

Figure 6. Effect of the starting potential on the performance of ORR: (a-c) Pd/C and (d-f) PdFe/rGO. (a) CVs (1600 rpm, 0.01 V s^{-1}) of the ring and disk of RRDE and the corresponding Tafel plots: (b) ECSA of Pd and (c) weight of Pd. (d) LSVs (1600 rpm, 0.005 V s^{-1}) of the ring and disk of RRDE and the corresponding Tafel plots: (e) ECSA of Pd and

(f) weight of Pd. Ring potential = 1200 mV_{RHE}. Electrolyte = 0.1 M KOH. Potentials were iR-drop corrected.

We finally evaluated the performance of the different materials towards ORR in an electrolytic solution of 0.1 M KOH. Figure 7a shows typical LSV profiles of ORR-RRDE, and Figures 7b-h display the different scenarios of comparison. Extended data are reported in Figures S18-S22. The disk current density increases with the rotation speed, but is not expected to significantly modify the fundamental data of E_{onset}, $E_{1/2}$, j_k, and n_{ex} (Eqs. 5-6); 1600 rpm is the most utilized value.[18] The rotation-rate dependent LSV profiles in Figures 7a, and S18-S22 show three regions of limitation, the kinetics (characterized by E_{onset}), the mixed kinetic-diffusion (characterized by $E_{1/2}$), and the mass transport (plateau characterized by j_{lim}, theoretically predicted by Eq. 6).

Taking into account the data before and after AST, the bimetallic-based catalysts of PdFe/Vulcan and PdFe/rGO have superior electrocatalytic performance with respect to other tested catalytic materials, whether home-made monometallic or the commercial Pd/C. Indeed, the most important aspect for an O_2-based cathode in FCs or metal-air batteries operating in alkaline environment has been how a given material will be active after a certain number of catalytic cycles. Specifically, Figure 7b reveals that, for all bimetallic-based electrodes, $E_{1/2}$ = 0.93 V_{RHE} after the AST protocol. The extracted key parameters are gathered in Table 3 and compared with the reported best performing nanoelectrocatalysts in Table S5. It is worth emphasizing that the cathode is expected to work above 0.7 V_{RHE} in order to generate a higher cell voltage ($U_{cell} = E_{cathode} - E_{anode}$), ideally higher than 0.8 V_{RHE} in H_2- or organic-fuelled fuel cells where the anode can be of 0.1-0.6 V_{RHE}. Interestingly, the yellowish region in Figure 7f shows a negligible amount of the by-product HO_2^- and so a maximum value of $n_{ex} \approx 4.0$ (faradaic efficiency of 100%). The value of the effectively transferred number of electrons per molecule of O_2 was further confirmed by both methods of Koutecky-Levich

(Figure 7g, mixed kinetic-diffusion region), and Levich (Figure 7h, diffusion-limiting region).[28,30,32] Basically, a higher amount of the hydrogen peroxide will not only decrease the faradaic efficiency immediately, but also and importantly, provokes the deterioration of the solid polymer membrane in long-term thus impacting the durability of the electrochemical device.

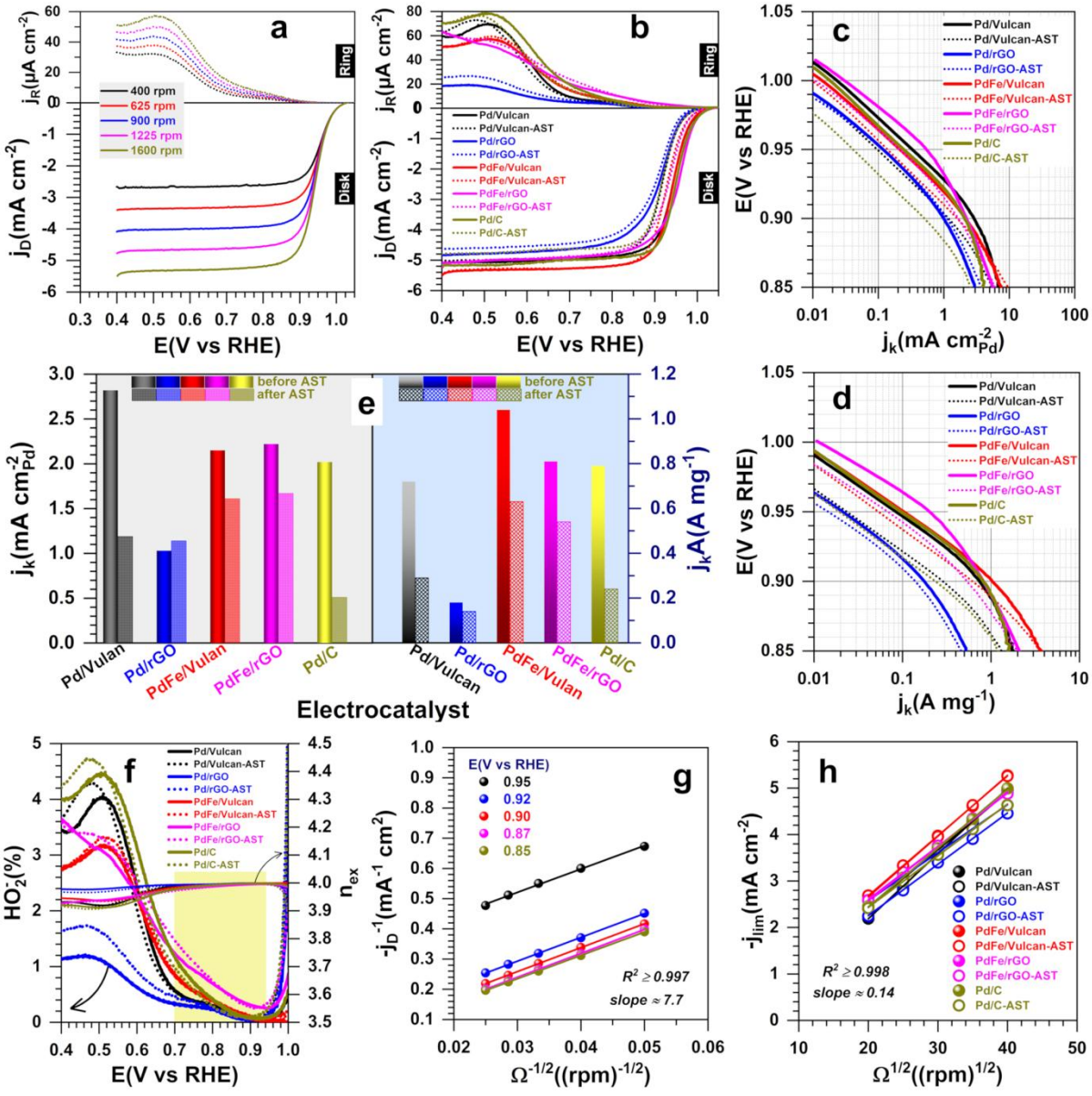

Figure 7. Electrochemical performance of ORR. (a) LSVs (1600 rpm, 0.005 V s^{-1}) of the ring and disk of RRDE curves of the PdFe/Vulcan material. (b) Comparative LSVs (1600 rpm, 0.005 V s^{-1}) before and after AST. (c, d) Tafel plots by (c) ECSA of palladium and (d)

weight of palladium. (e) Comparative kinetic current density at 900 mV_{RHE}: by ECSA of Pd (left) and Pd weight (right). (f) HO_2^- % (left) and n_{ex} (right). (g) Koutecky-Levich plots at 950, 920, 900, 870, and 850 mV_{RHE} for the PdFe/Vulcan material. (h) Comparative Levich plots at 700 mV_{RHE}. The ring potential was fixed at 1200 mV_{RHE}. Electrolyte = KOH at a concentration of 0.1 M. The potentials were iR-drop corrected.

For comparison, at 900 mV_{RHE}, the achieved j_k(A mg^{-1}_{Pd}) = 1.04 (PdFe/Vulcan), and 0.81 (PdFe/rGO) are 5.2-10.7 times higher than the reported nanoalloys of Pd_3Fe/C (j_k = 0.097 A mg^{-1}_{Pd}),[3] and PdFe/C (j_k = 0.157 A mg^{-1}_{Pd}).[44] In resume, the obtained j_k = 2.2 mA cm^{-2}_{Pd} (1.04 A mg^{-1}_{Pd}) at 900 mV_{RHE} is significantly larger than the majority of the reports of j_k = 0.05-3.7 mA $cm^{-2}_{noble\text{-}metal}$ (0.04-2.0 A $mg^{-1}_{noble\text{-}metal}$) for anodic direction,[3,13-14,16-17] and j_k = 0.2-0.6 mA $cm^{-2}_{noble\text{-}metal}$ (0.08-2.0 A $mg^{-1}_{noble\text{-}metal}$) for the unspecified direction.[22-24] Those data do not include the unprecedented record of j_k = 11.6 mA cm^{-2}_{Pd} (16.4 A mg^{-1}_{Pd}) for PdMo-bimetallene/C and where the performance of Pd-metallene/C (j_k = 0.48 mA cm^{-2}_{Pd} or 0.65 A mg^{-1}_{Pd}) was well below the monometallic Pd/Vulcan synthesized by the present method (j_k = 2.82 mA cm^{-2}_{Pd} or 0.72 A mg^{-1}_{Pd}). The driving force underlying this excellent enhancement in the electrocatalytic efficiency of the engineered nanocatalysts are the same as those previously discussed in the study of the glycerol oxidation and CO stripping. Earlier theoretical calculations have suggested that the enhancement of the catalytic activity of Pd-based materials towards ORR originates from the modification of the distance of the Pd-Pd bond induced by the presence of a foreign atom that results in a modification of the electron configuration, which is responsible for the catalytic properties.[51-52]

Table 3. Performance metrics of Pd/C (commercial), and as-fabricated electrocatalysts before and after AST: Electrolyte = KOH at 0.1 M; ORR (RRDE's speed =1600 rpm;

LSV's scan rate = 0.005 V s^{-1}). HO_2^-(%) and n_{ex} were determined at 850 V_{RHE}. j_k was determined at 900 mV_{RHE}.

Entry	Pd/Vulcan		Pd/rGO		PdFe/Vulcan		PdFe/rGO		Pd/C	
	Before	After	Before	After	Before	After	Before	After	Before	After
ECSA(m^2 g^{-1})	26	24	17	13	39	31	30	25	48	56
E_{onset}(V_{RHE})	1.04	1.02	1.01	1.00	1.03	1.03	1.04	1.03	1.04	1.00
$E_{1/2}$(V_{RHE})	0.94	0.92	0.91	0.90	0.94	0.93	0.95	0.93	0.94	0.91
j_k(mA cm^{-2}_{Pd})	2.82	1.19	1.03	1.14	2.15	1.61	2.22	1.67	2.02	0.51
j_k(A mg^{-1}_{Pd})	0.72	0.29	0.18	0.14	1.04	0.63	0.81	0.54	0.79	0.24
b(mV dec^{-1})	44	45	51	50	45	47	40	43	45	46
HO_2^-(%)	0.16	0.13	0.09	0.10	0.21	0.22	0.49	0.48	0.19	0.13
n_{ex}	3.996	3.997	3.998	3.998	3.995	3.995	3.990	3.990	3.996	3.997

3.5. Theoretical, computational, and electroanalytical investigations

In order to gain insight in the atomic ordering in PdFe nanoalloy catalysts and their interaction with the glycerol molecule, we studied the segregation behavior of one Fe layer in PdFe(111) surface in absence and presence of adsorbate. Indeed, the previous physicochemical characterizations show that the facet (111) is dominant. The segregation energy (E_{seg}) of one Fe layer (9 atoms) in the PdFe(111) is defined by Eq. 8.

$$E_{seg} = [E(PdFe(111)_{(Fe\ x\text{-}layer)}) - E(PdFe(111)_{(Fe\ 4th\text{-}layer)})]/9 \quad \text{(Eq. 8)}$$

In Eq. 8, $E(PdFe(111)_{(Fe\ x\text{-}layer)})$ represents the total energy of the PdFe(111) surface with Fe located in the upper surface layers (x-layer = 1, 2 or 3), and $E(PdFe(111)_{(Fe\ 4th\text{-}layer)})$ represents the total energy of PdFe(111) with the Fe located in the 4^{th} layer of the slab, which corresponds to the presence of Fe in the bulk. Negative values of E_{seg} indicate surface segregation while positive values indicate bulk segregation.[37,47-48,58-59] Figure 8a presents the evolution of segregation energies of Fe layer as a function of its position in PdFe(111) slab in

absence and in presence of adsorbed glycerol molecule. Under vacuum conditions, i.e. in absence of any adsorbate (full line), the DFT-D3 results show positive segregation energy of Fe located on the PdFe(111) top most surface layer. This indicates that iron is not stable at the top most surface layer and that Pd surface segregation is preferred. The higher stability of Pd rather than Fe on the surface of PdFe(111) is expected as Pd has lower surface energy (2 J m^{-2}) than Fe (2.41 J m^{-2}).[60] In addition to surface energies, the stronger cohesive energy of iron (10% higher) and the lower atomic radius (26% lower) compared to Pd[60] are also driving forces[61] that may explain the surface segregation of Pd. Interestingly, analyzing the preferred iron location, it appears that the first sub-surface layer of PdFe(111) i.e. the second layer of the slab, offers better stability rather than the bulk (E_{seg} = -0.12 eV). The energetically favorable location of Fe at the sub-surface layer of PdFe(111) slab can be understood by two effects: not being on the topmost surface layer can avoid the higher surface energy of Fe while the near surface location allows the system to release the elastic energy due to the atomic size mismatch. This size effect was already reported for the case of AuCu nanalloys.[62] DFT-D3 geometry optimizations show that the location of Fe in the sub-surface layer induces atomic contraction of 0.7% on the surface Pd-Pd distance, decreasing from 2.73 Å to 2.71 Å.

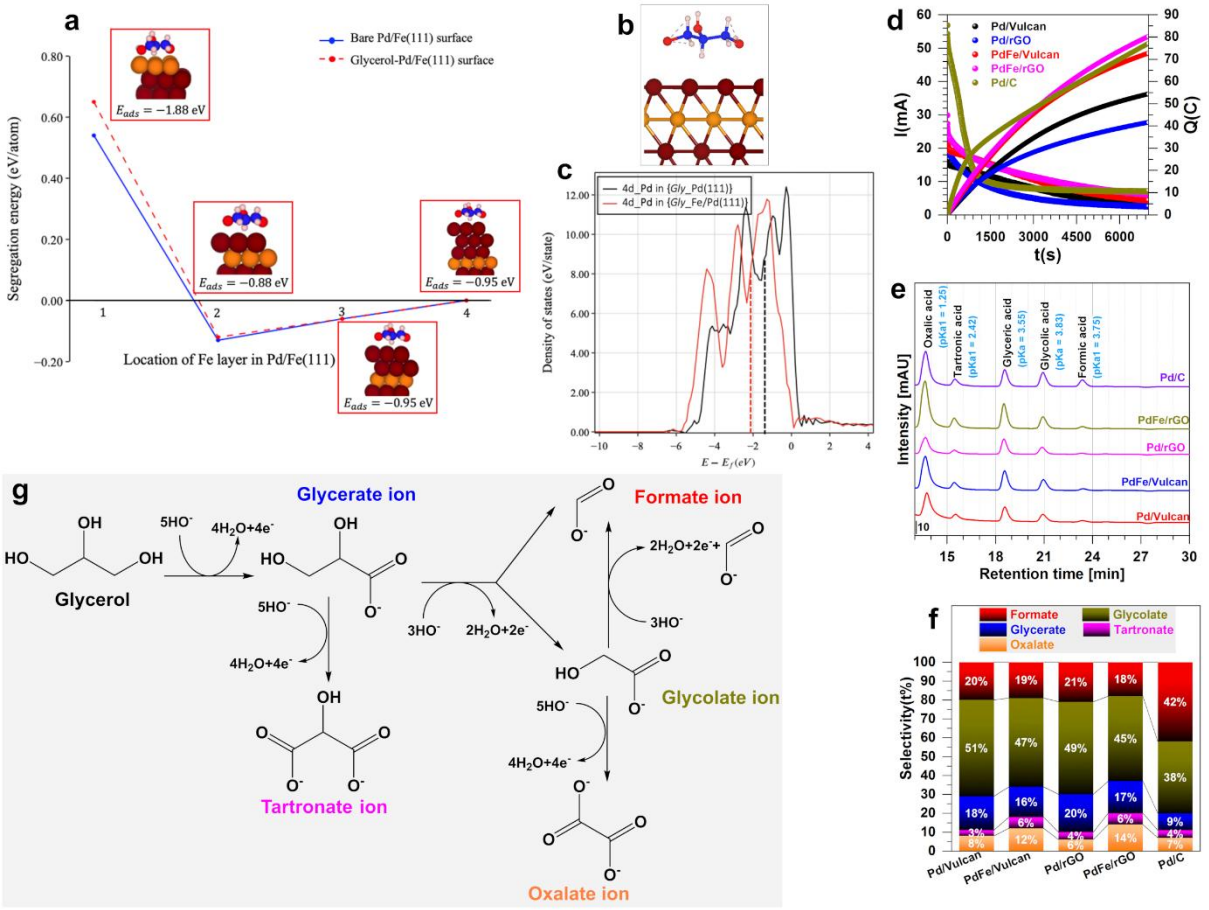

Figure 8. (a) Evolution of the segregation energies (E_{seg}) (eV/Fe atom) of one-layer Fe from the Pd ‘‘bulk’’ (4th layer in the sub-surface) to the first surface layer: DFT-D3 calculations were performed in the absence (full-line) and presence (dashed line) of one adsorbed glycerol molecule (see insert). (b) Illustration of the adsorption mode Glycerol on the PdFe(111) surface. (c) Local Density of States DOSs (states/eV) of the Pd d-bands in Pd(111) (black line) and in PdFe(111) with Fe located in the subsurface layer (colored lines). Dashed vertical lines correspond to the d-band centers relative to the Fermi energy ($E - E_{Fermi}$ (eV)). (d) Evolution of the oxidation current (I, left y-axis) and quantity of electricity (Q, right y-axis) during a 2 h long electrolysis (1 M KOH, 0.1 M glycerol) at 0.8 V vs RHE (no iR-drop correction). (e) Chromatograms from HPLC analysis after electrolysis. (f) The products distribution after electrolysis. (g) Reaction pathways proposed to account the oxidation of glycerol on the as-synthesized nanocatalysts in alkaline media.

In the literature, there were several theoretical works devoted to the analysis of the interaction of glycerol with closed packed transition metal surfaces.[63-65] To the best of our knowledge, the interaction of glycerol and its effect on the surface of Pd-based nanoalloys have never been investigated. Herein, we report our first DFT investigations on the system. Figure 8b reports the segregation energy evolution of Fe in PdFe(111) in presence of adsorbed glycerol (dashed line). Except a very slight decrease of (0.09 eV/atom) for the computed E_{seg} of Fe layer located on the top most surface, the segregation behavior remains similar to the one calculated under vacuum conditions. This result indicates that the adsorbate has negligible effect on the segregation behavior of iron. The adsorbed glycerol molecule is found to bind through two O atoms near on-top adsorption sites of PdFe(111) and Pd(111) surfaces (Figure 8b). In addition, one hydrogen from the carbon chain, almost parallel to the surface, is found to point towards the surface with a distance of H-Pd of 2.26 Å. To calculate the adsorption energies of glycerol on the surface, Eq. 9 was used.

$$E_{ads} = E_{slab+Gly} - E_{slab} - E_{gly\_gas} \quad \text{(Eq. 9)}$$

In Eq. 9, $E_{slab+Gly}$ is the total energy of glycerol adsorbed on Pd(111) or PdFe(111) slab surface, and E_{gly_gas} and E_{slab} are the total energies of free glycerol and clean slab surface, respectively. The adsorption energy of glycerol molecule on Pd(111) is calculated to be of -1.20 eV, which is in line with recent DFT results of Mendes et al.[63] In presence of Fe in the top most surface layer of PdFe(111) (see inserts in Figure 8a), the adsorption energy of glycerol downshift by 0.68 eV ($E_{ads\ Gly}$ = -1.88 eV), which indicates a strong affinity of glycerol to Fe. When Fe is located in the first subsurface layer and in the bulk (third and fourth subsurface layers), the adsorption energies upshift to -0.88 eV and -0.95 eV, respectively. Interestingly, these results showing on one hand the strong affinity between glycerol and Fe and on the other hand the stabilization of Fe at the sub-surface layer (2nd

layer) rather than on the top surface layer, are counterintuitive. Indeed, the expected response to adsorbates is that the more reactive alloy component (i.e., the one interacting strongly with the adsorbates) segregates to the surface.[66] For our system, this simplistic picture does not take into account the specificities of the segregating atoms where elastic release is required. In addition, the stabilization of Fe in the subsurface layer allows moderate adsorption of reactant molecules which may explain the highly improved catalytic properties of PdFe nanocatalysts. In Figure 8c are reported the local density of states (LDOSs) of the d-band of Pd surface in Pd(111) and PdFe(111) with Fe located in the first subsurface layer. These densities are an important quantity for understanding the bonding in a compound. According to the d-band model developed by Nørskov,[67-68] the position of the *d*-band center relative to the Fermi level is the main parameter controlling adsorption. When Fe is located at the sub-surface layer, the *d*-band center of Pd is found to shift away from the Fermi level by 0.68 eV. This shift indicates a decrease in the density of available *d* states and therefore explains the decrease of the adsorption energy of glycerol on Pd in presence of Fe. These theoretical results confirm the previous experimental findings. For ORR, these DFT calculations definitely tell that the driving force behind the ultrafast kinetics of the synthesized $Pd_{0.8}Fe_{0.2}$ materials is the Pd_{core}-Fe-Pd_{skin} structure, similar Pt-skin surfaces of Pt_3Ni.[47-48]

We finally conducted an electroanalytical investigation to find the reaction products in order to deeply account the glycerol oxidation mechanism. Figure 8d of the time dependent current and charge during the electrolysis highlights the drastically improved efficiency of the bimetallic PdFe over the monometallic Pd, and the commercial Pd/C (-80% activity after 20 min). The identified reaction products by HPLC (Figures 8e, and S23) are shown in Figure 8f in terms of the selectivity; all quantitative metrics are reported in Tables S6-S7. Among the five products (to compare, up to nine products were reported[9]), the main reaction products are glycolate, formate, and glycerol; lactate was not detected contrary to recent report of Lima et

al.[8] Based on these findings (no carbonate from full C-C bond cleavage was detected), a scheme was proposed (Figure 8g). Given the high amount of formate (42%) at the commercial Pd/C, the carbon-carbon bond is easily broken at this catalyst than the as-synthesized material (18-21%). Also, the commercial Pd/C has a moderate faradaic efficiency of 78% whereas the developed electrocatalysts show high values of 83-99%. It can be specifically observed that the presence of iron substantially promotes the formation of tartronate and oxalate as products. And therefore better selectivity towards dicarboxylate compounds thanks to the favorable adsorption of the reactants/intermediates.

4. Conclusion

We report herein Pd-based nanoparticles as multifunctional nanocatalysts for the key reactions of glycerol oxidation and O_2 reduction (ORR) in an alkaline environment. We have conducted extensive studies by physicochemical (XRD, ICP-OES, TEM, STEM-EDX, XPS), electrochemical (RRDE, CV, CA, EIS), electroanalytical (HPLC), and theoretical (DFT) methods to unveil the effects of the second atom (Fe) on the properties of the as-synthesized nanomaterials. Our novelty is to report a complete study compared to existing literature where Pd-Fe supported onto Vulcan or rGO was most often used separately for ORR and glycerol oxidation, which makes the results difficult to compare because of different conditions of preparation/testing and absence of DFT calculations. Also, our synthesis method allowed to produce bare (ligand-free) bimetallic PdFe electrocatalysts with clean catalytic surface without any contamination of organic capping agent or surfactant in order to maximize the number of available active sites. Our findings show that, for glycerol electrooxidation, the developed catalysts have lower starting potential (E_{onset} = 520 mV_{RHE}) than the run commercial catalyst Pd/C (E_{onset} = 580 mV_{RHE}). The observed synergic effect in PdFe/rGO bimetallic catalyst during the CO stripping was confirmed for glycerol

electrooxidation with j_p = 2.3 mA cm^{-2}_{Pd} = 1.11 A mg^{-1}_{Pd} at the peak current density, which outperformed the benchmark Pd/C (j_p = 0.47 mA cm^{-2}_{Pd} (0.39 A mg^{-1}_{Pd})) and the majority of the reported catalysts. Glycolate is the main reaction product. The investigation enlightens us on the strong effect of the direction of the potential scanning on the magnitude of the measured kinetic parameters of ORR (E_{onset}, $E_{1/2}$, and j_k). However, this does not change the reaction product nature, which was OH^- in a direct 4-electron process, thus a maximum faradaic efficiency of 100%. Specifically, the anodic sweep of the potential produces the best results with positive shift of $\Delta E_{1/2,anodic/cathodic}$ = 60 mV from the cathodic direction to the anode one as well as the huge augmentation of $j_{k,anodic}$ = 19.0×, 6.9×, 3.4×, and 2.4×$j_{k,cathodic}$ at 950, 900, 870, and 850 mV_{RHE}, respectively. These outcomes that confirm earlier observations at Pt surface in acidic media consequently recommend that any report of ORR performance should clearly indicate the used direction to record the data in order to avoid conflicting comparison, wherein the kinetic metrics could be over- or under-estimated. Finally, the synthesized catalysts showed a particularly high j_k of 2 mA cm^{-2}_{Pd} and 1 A mg^{-1}_{Pd}, which were found to largely exceed the commercial Pd/C and the existing literature, thus contributing to the advancement of the electrochemical energy production and storage technologies.

ASSOCIATED CONTENT

Supporting Information. The following files are available free of charge. Additional experimental details, materials, and methods on the fundamentals of ORR at RRDE; comparison of the performance of relevant metallic catalysts for the glycerol electrooxidation reaction in alkaline media from literature; comparison of the performance of relevant metallic catalysts for the ORR in alkaline media from literature, TEM/STEM/EDX images of Pd-based electrocatalysts; survey XPS spectra of the as-synthesized Pd-based

nanomaterials; electrocatalytic behavior of as-synthesized Pd-based nanomaterials for ORR and glycerol oxidation; chromatograms obtained from HPLC analysis of standards and reaction solutions (file type, i.e., PDF)

AUTHOR INFORMATION

Corresponding Author

*S.T. E-mail: sophie.tingry@umontpellier.fr

*D.C.: E-mail: david.cornu@enscm.fr

*Y.H.: yaovi.holade@enscm.fr

Author Contributions

The manuscript was written through contributions of all authors. All authors have given approval to the final version of the manuscript. ‡These authors contributed equally.

Notes

The authors declare no competing financial interest.

ACKNOWLEDGMENT

Y. H. acknowledge startup funds support from European Institute of Membranes of Montpellier (France) through (COGENFC – PAT-Energy-Axis-2018), and LabEx CheMISyst (ANR-10-LABX-05-01) as well as Cabot Corporation (Europe, Middle East & Africa; SIA Cabot Latvia, Latvia) for providing VULCAN® XC72R. Magalie Lefeuvre (*Laboratoire de Mesures Physiques*, LMP), Valérie Flaud (Nacelle XPS), and Erwan Oliviero (PLateforme MEA) of the University of Montpellier (France) are acknowledged for CHNS-O, XPS and TEM-based analysis, respectively.

REFERENCES

(1) Verma, S.; Lu, S.; Kenis, P. J. A., Co-Electrolysis of CO_2 and Glycerol as a Pathway to Carbon Chemicals with Improved Technoeconomics due to Low Electricity Consumption. *Nat. Energy* **2019,** *4*, 466-474.

(2) Garcia, A. C.; Caliman, J.; Ferreira, E. B.; Tremiliosi-Filho, G.; Linares, J. J., Promotional Effect of Ag on the Catalytic Activity of Au for Glycerol Electrooxidation in Alkaline Medium. *ChemElectroChem* **2015,** *2*, 1036-1041.

(3) Cui, Z.; Li, L.; Manthiram, A.; Goodenough, J. B., Enhanced Cycling Stability of Hybrid Li–Air Batteries Enabled by Ordered Pd_3Fe Intermetallic Electrocatalyst. *J. Am. Chem. Soc.* **2015,** *137*, 7278-7281.

(4) Stamenkovic, V. R.; Strmcnik, D.; Lopes, P. P.; Markovic, N. M., Energy and Fuels from Electrochemical Interfaces. *Nat. Mater.* **2017,** *16*, 57-69.

(5) Ghosh, S.; Bera, S.; Bysakh, S.; Basu, R. N., Highly Active Multimetallic Palladium Nanoalloys Embedded in Conducting Polymer as Anode Catalyst for Electrooxidation of Ethanol. *ACS Appl. Mater. Interfaces.* **2017,** *9*, 33775-33790.

(6) Li, S.; Lai, J.; Luque, R.; Xu, G., Designed Multimetallic Pd Nanosponges with Enhanced Electrocatalytic Activity for Ethylene Glycol and Glycerol Oxidation. *Energy Environ. Sci.* **2016,** *9*, 3097-3102.

(7) de Souza, M. B. C.; Yukuhiro, V. Y.; Vicente, R. A.; Vilela Menegaz Teixeira Pires, C. T. G.; Bott-Neto, J. L.; Fernández, P. S., Pb- and Bi-Modified Pt Electrodes toward Glycerol Electrooxidation in Alkaline Media. Activity, Selectivity, and the Importance of the Pt Atoms Arrangement. *ACS Catal.* **2020,** *10*, 2131-2137.

(8) Lima, C. C.; Rodrigues, M. V. F.; Neto, A. F. M.; Zanata, C. R.; Pires, C. T. G. V. M. T.; Costa, L. S.; Solla-Gullón, J.; Fernández, P. S., Highly Active Ag/C Nanoparticles Containing Ultra-Low Quantities of Sub-Surface Pt for the Electrooxidation of Glycerol in Alkaline Media. *Appl. Catal. B: Env.* **2020,** *279*, Article Number: 119369.

(9) Zhou, Y.; Shen, Y.; Xi, J., Seed-Mediated Synthesis of Pt_xAu_y@Ag Electrocatalysts for the Selective Oxidation of Glycerol. *Appl. Catal. B: Env.* **2019,** *245*, 604-612.

(10) Du, H.; Wang, K.; Tsiakaras, P.; Shen, P. K., Excavated and Dendritic Pt-Co Nanocubes as Efficient Ethylene Glycol and Glycerol Oxidation Electrocatalysts. *Appl. Catal. B: Env.* **2019,** *258*, Article Number: 117951.

(11) Boukil, R.; Tuleushova, N.; Cot, D.; Rebiere, B.; Bonniol, V.; Cambedouzou, J.; Tingry, S.; Cornu, D.; Holade, Y., Enhanced Electrocatalytic Activity and Selectivity of Glycerol Oxidation Triggered by Nanoalloyed Silver–Gold Nanocages Directly Grown on Gas Diffusion Electrodes. *J. Mater. Chem. A* **2020,** *8*, 8848-8856.

(12) Chen, Z.; Liu, C.; Zhao, X.; Yan, H.; Li, J.; Lyu, P.; Du, Y.; Xi, S.; Chi, K.; Chi, X.; Xu, H.; Li, X.; Fu, W.; Leng, K.; Pennycook, S. J.; Wang, S.; Loh, K. P., Promoted Glycerol Oxidation Reaction in an Interface-Confined Hierarchically Structured Catalyst. *Adv. Mater.* **2019,** *31*, 1804763.

(13) Zhu, W.; Yuan, H.; Liao, F.; Shen, Y.; Shi, H.; Shi, Y.; Xu, L.; Ma, M.; Shao, M., Strain Engineering for Janus Palladium-Gold Bimetallic Nanoparticles: Enhanced Electrocatalytic Performance for Oxygen Reduction Reaction and Zinc-Air Battery. *Chem. Eng. J.* **2020,** *389*, 124240.

(14) Lu, X.; Ahmadi, M.; DiSalvo, F. J.; Abruña, H. D., Enhancing the Electrocatalytic Activity of Pd/M (M = Ni, Mn) Nanoparticles for the Oxygen Reduction Reaction in Alkaline Media through Electrochemical Dealloying. *ACS Catal.* **2020,** *10*, 5891-5898.

(15) Luo, M.; Zhao, Z.; Zhang, Y.; Sun, Y.; Xing, Y.; Lv, F.; Yang, Y.; Zhang, X.; Hwang, S.; Qin, Y.; Ma, J.-Y.; Lin, F.; Su, D.; Lu, G.; Guo, S., PdMo Bimetallene for Oxygen Reduction Catalysis. *Nature* **2019,** *574*, 81-85.

(16) Yang, H.; Wang, K.; Tang, Z.; Liu, Z.; Chen, S., Bimetallic PdZn Nanoparticles for Oxygen Reduction Reaction in Alkaline Medium: The Effects of Surface Structure. *J. Catal.* **2020,** *382*, 181-191.
(17) Zhang, X.; Fan, J.; Han, M.; Zhao, S.; Lu, L.; Xu, D.; Lin, Y.; Shi, N.; Liu, Y.; Lan, Y.-Q.; Bao, J.; Dai, Z., Versatile Synthesis of Pd−M (M=Cr, Mo, W) Alloy Nanosheets Flower-like Superstructures for Efficient Oxygen Reduction Electrocatalysis. *ChemCatChem* **2020,** *12*, 4138–4148.
(18) Shinozaki, K.; Zack, J. W.; Richards, R. M.; Pivovar, B. S.; Kocha, S. S., Oxygen Reduction Reaction Measurements on Platinum Electrocatalysts Utilizing Rotating Disk Electrode Technique: I. Impact of Impurities, Measurement Protocols and Applied Corrections. *J. Electrochem. Soc.* **2015,** *162*, F1144-F1158.
(19) Holade, Y.; da Silva, R. G.; Servat, K.; Napporn, T. W.; Canaff, C.; De Andrade, A. R.; Kokoh, K. B., Facile Synthesis of Highly Active and Durable PdM/C (M = Fe, Mn) Nanocatalysts for the Oxygen Reduction Reaction in an Alkaline Medium. *J. Mater. Chem. A* **2016,** *4*, 8337-8349.
(20) Yang, Y.; Xiao, W.; Feng, X.; Xiong, Y.; Gong, M.; Shen, T.; Lu, Y.; Abruña, H. D.; Wang, D., Golden Palladium Zinc Ordered Intermetallics as Oxygen Reduction Electrocatalysts. *ACS Nano* **2019,** *13*, 5968-5974.
(21) Inaba, M.; Jensen, A. W.; Sievers, G. W.; Escudero-Escribano, M.; Zana, A.; Arenz, M., Benchmarking High Surface Area Electrocatalysts in a Gas Diffusion Electrode: Measurement of Oxygen Reduction Activities Under Realistic Conditions. *Energy Environ. Sci.* **2018,** *11*, 988-994.
(22) Wang, H.; Abruña, H. D., Single-phase $Ru_{1-x-y}Mn_xCo_yO_2$ nanoparticles as Highly Effective Oxygen Reduction Electrocatalysts in Alkaline Media with enhanced stability and Fuel-Tolerance. *Appl. Catal. B: Env.* **2020,** *277*, 119149.
(23) Hu, Y.; Lu, Y.; Zhao, X.; Shen, T.; Zhao, T.; Gong, M.; Chen, K.; Lai, C.; Zhang, J.; Xin, H. L.; Wang, D., Highly active N-Doped Carbon Encapsulated Pd-Fe Intermetallic Nanoparticles for the Oxygen Reduction Reaction. *Nano Res.* **2020,** *13*, 2365-2370.
(24) Liu, X.-J.; Yin, X.; Sun, Y.-D.; Yu, F.-J.; Gao, X.-W.; Fu, L.-J.; Wu, Y.-P.; Chen, Y.-H., Interlaced Pd–Ag Nanowires Rich in Grain Boundary Defects for Boosting Oxygen Reduction Electrocatalysis. *Nanoscale* **2020,** *12*, 5368-5373.
(25) Marcano, D. C.; Kosynkin, D. V.; Berlin, J. M.; Sinitskii, A.; Sun, Z.; Slesarev, A.; Alemany, L. B.; Lu, W.; Tour, J. M., Improved Synthesis of Graphene Oxide. *ACS Nano* **2010,** *4*, 4806-4814.
(26) Kumar, K.; Canaff, C.; Rousseau, J.; Arrii-Clacens, S.; Napporn, T. W.; Habrioux, A.; Kokoh, K. B., Effect of the Oxide–Carbon Heterointerface on the Activity of Co_3O_4/NRGO Nanocomposites toward ORR and OER. *J. Phys. Chem. C* **2016,** *120*, 7949-7958.
(27) Holade, Y.; Morais, C.; Servat, K.; Napporn, T. W.; Kokoh, K. B., Enhancing the Available Specific Surface Area of Carbon Supports to Boost The Electroactivity of Nanostructured Pt Catalysts. *Phys. Chem. Chem. Phys.* **2014,** *16*, 25609-25620.
(28) Napporn, T. W.; Holade, Y.; Kokoh, B.; Mitsushima, S.; Mayer, K.; Eichberger, B.; Hacker, V. In *Fuel Cells and Hydrogen: From Fundamentals to Applied Research*, Hacker, V., Mitsushima, S., Eds. Elsevier: 2018; pp 175-214.
(29) Vork, F. T. A.; Barendrecht, E., The reduction of dioxygen at Polypyrrole-Modified Electrodes with Incorporated Pt Particles. *Electrochim. Acta* **1990,** *35*, 135-139.
(30) Gileadi, E., *Electrods Kinetics for Chemists, Chemical Engineers, and Materials Scientists*. Wiley-VCH: New York, N Y, USA, 1993; p 616.
(31) Gubbins, K. E.; Walker, R. D., The Solubility and Diffusivity of Oxygen in Electrolytic Solutions. *J. Electrochem. Soc.* **1965,** *112*, 469-471.

(32) Xing, W.; Yin, G.; Zhang, J., *Rotating Electrode Methods and Oxygen Reduction Electrocatalysts*. 1 ed.; Elsevier Science and Technology: Poland, 2014; p 322.
(33) Perdew, J. P.; Wang, Y., Accurate and Simple Analytic Representation of the Electron-Gas Correlation Energy. *Phys. Rev. B* **1992,** *45*, 13244-13249.
(34) Kresse, G.; Hafner, J., Ab Initio Molecular Dynamics for Liquid Metals. *Phys. Rev. B* **1993,** *47*, 558-561.
(35) Blöchl, P. E.; Jepsen, O.; Andersen, O. K., Improved Tetrahedron Method For Brillouin-Zone Integrations. *Phys. Rev. B* **1994,** *49*, 16223-16233.
(36) Kresse, G.; Joubert, D., From Ultrasoft Pseudopotentials to the Projector Augmented-Wave Method. *Phys. Rev. B* **1999,** *59*, 1758-1775.
(37) Grimme, S.; Antony, J.; Ehrlich, S.; Krieg, H., A Consistent and Accurate ab Initio Parametrization of Density Functional Dispersion Correction (DFT-D) for the 94 Elements H-Pu. *J. Chem. Phys.* **2010,** *132*, 154104.
(38) Krishnankutty, N.; Vannice, M. A., Effect of Pretreatment on Surface Area, Porosity, and Adsorption Properties of a Carbon Black. *Chem. Mater.* **1995,** *7*, 754-763.
(39) Abidat, I.; Cazayus, E.; Loupias, L.; Morais, C.; Comminges, C.; Napporn, T. W.; Portehault, D.; Durupthy, O.; Mamede, A.-S.; Chanéac, C.; Lamonier, J.-F.; Habrioux, A.; Kokoh, K. B., Co_3O_4/rGO Catalysts for Oxygen Electrocatalysis: On the Role of the Oxide/Carbon Interaction. *J. Electrochem. Soc.* **2019,** *166*, H94-H102.
(40) Moon, I. K.; Lee, J.; Ruoff, R. S.; Lee, H., Reduced Graphene Oxide By Chemical Graphitization. *Nat. Commun.* **2010,** *1*, 73.
(41) Feng, H.; Cheng, R.; Zhao, X.; Duan, X.; Li, J., A low-temperature method to Produce Highly Reduced Graphene Oxide. *Nat. Commun.* **2013,** *4*, 1539.
(42) Palma, L. M.; Almeida, T. S.; Oliveira, V. L.; Tremiliosi-Filho, G.; Gonzalez, E. R.; de Andrade, A. R.; Servat, K.; Morais, C.; Napporn, T. W.; Kokoh, K. B., Identification of Chemicals Resulted in Selective Glycerol Conversion as Sustainable Fuel on Pd-based Anode Nanocatalysts. *RSC Adv.* **2014,** *4*, 64476-64483.
(43) Ghosh, S.; Bysakh, S.; Basu, R. N., Bimetallic $Pd_{96}Fe_4$ Nanodendrites Embedded in Graphitic Carbon Nanosheets as Highly Efficient Anode Electrocatalysts. *Nanoscale Advances* **2019,** *1*, 3929-3940.
(44) Zhang, Z.; More, K. L.; Sun, K.; Wu, Z.; Li, W., Preparation and Characterization of PdFe Nanoleaves as Electrocatalysts for Oxygen Reduction Reaction. *Chem. Mater.* **2011,** *23*, 1570-1577.
(45) Da Silva, R. G.; Aquino Neto, S.; Kokoh, K. B.; De Andrade, A. R., Electroconversion of Glycerol in Alkaline Medium: From Generation of Energy to Formation of Value-Added Products. *J. Power Sources* **2017,** *351*, 174-182.
(46) Bandarenka, A. S.; Koper, M. T. M., Structural and electronic effects in Heterogeneous Electrocatalysis: Toward a Rational Design of Electrocatalysts. *J. Catal.* **2013,** *308*, 11-24.
(47) Stamenkovic, V. R.; Fowler, B.; Mun, B. S.; Wang, G.; Ross, P. N.; Lucas, C. A.; Marković, N. M., Improved Oxygen Reduction Activity on $Pt_3Ni(111)$ via Increased Surface Site Availability. *Science* **2007,** *315*, 493-497.
(48) Stamenkovic, V. R.; Mun, B. S.; Mayrhofer, K. J. J.; Ross, P. N.; Markovic, N. M., Effect of Surface Composition on Electronic Structure, Stability, and Electrocatalytic Properties of Pt-Transition Metal Alloys: Pt-Skin versus Pt-Skeleton Surfaces. *J. Am. Chem. Soc.* **2006,** *128*, 8813-8819.
(49) Kibis, L. S.; Stadnichenko, A. I.; Koscheev, S. V.; Zaikovskii, V. I.; Boronin, A. I., Highly Oxidized Palladium Nanoparticles Comprising Pd^{4+} Species: Spectroscopic and Structural Aspects, Thermal Stability, and Reactivity. *J. Phys. Chem. C* **2012,** *116*, 19342-19348.

(50) Kim, K. S.; Gossmann, A. F.; Winograd, N., X-ray Photoelectron Spectroscopic Studies of Palladium Oxides and the Palladium-Oxygen Electrode. *Anal. Chem.* **1974,** *46*, 197-200.
(51) Shao, M.; Liu, P.; Zhang, J.; Adzic, R., Origin of Enhanced Activity in Palladium Alloy Electrocatalysts for Oxygen Reduction Reaction. *J. Phys. Chem. B* **2007,** *111*, 6772-6775.
(52) Fernández, J. L.; Walsh, D. A.; Bard, A. J., Thermodynamic Guidelines for the Design of Bimetallic Catalysts for Oxygen Electroreduction and Rapid Screening by Scanning Electrochemical Microscopy. M−Co (M: Pd, Ag, Au). *J. Am. Chem. Soc.* **2005,** *127*, 357-365.
(53) Kurbatov, G.; Darque-Ceretti, E.; Aucouturier, M., Characterization of Hydroxylated Oxide Film on Iron Surfaces and its Acid–Base Properties using XPS. *Surf. Interface Anal.* **1992,** *18*, 811-820.
(54) Holade, Y.; Napporn, T. W.; Morais, C.; Servat, K.; Kokoh, K. B., Probing Structure Modification of Palladium Nanomaterials during Chemical Synthesis by using In Situ X-ray Diffraction: Electrochemical Properties. *ChemElectroChem* **2015,** *2*, 592–599.
(55) López-Cudero, A.; Cuesta, Á.; Gutiérrez, C., Potential Dependence of the Saturation CO Coverage of Pt Electrodes: The Origin of the Pre-peak in CO-Stripping Voltammograms. Part 2: Pt(100). *J. Electroanal. Chem.* **2006,** *586*, 204-216.
(56) Orazem, M. E.; Tribollet, B., *Electrochemical Impedance Spectroscopy*. 2 ed.; John Wiley & Sons, Inc. : Hoboken, New Jersey, USA, 2017; p 367.
(57) Parpot, P.; Kokoh, K. B.; Beden, B.; Lamy, C., Electrocatalytic Oxidation of Saccharose in Alkaline Medium. *Electrochim. Acta* **1993,** *38*, 1679-1683.
(58) Juárez, M. F.; Soldano, G.; Guesmi, H.; Tielens, F.; Santos, E., Catalytic Properties of Au Electrodes Modified by an Underlayer of Pd. *Surf. Sci.* **2015,** *631*, 235-247.
(59) Zhu, B.; Creuze, J.; Mottet, C.; Legrand, B.; Guesmi, H., CO Adsorption-Induced Surface Segregation and Formation of Pd Chains on AuPd(100) Alloy: Density Functional Theory Based Ising Model and Monte Carlo Simulations. *J. Phys. Chem. C* **2016,** *120*, 350-359.
(60) Mills, K. C.; Su, Y. C., Review of Surface Tension data for Metallic Elements and Alloys: Part 1 – Pure Metals. *Int. Mater. Rev.* **2006,** *51*, 329-351.
(61) Creuze, J.; Guesmi, H.; Mottet, C.; Zhu, B.; Legrand, B., Surface Segregation in AuPd Alloys: Ab Initio Analysis of the Driving Forces. *Surf. Sci.* **2015,** *639*, 48-53.
(62) Dhifallah, M.; Dhouib, A.; Aldulaijan, S.; Renzo, F. D. I.; Guesmi, H., First-Principles Study of Au–Cu Alloy Surface Changes Induced By Gas Adsorption of CO, NO, or O_2. *J. Chem. Phys.* **2016,** *145*, 024701.
(63) Mendes, P. C. D.; Costa-Amaral, R.; Gomes, J. F.; Da Silva, J. L. F., The Influence of Hydroxy Groups on the Adsorption of Three-Carbon Alcohols on Ni(111), Pd(111) and Pt(111) surfaces: A Density Functional Theory Study within the D3 Dispersion Correction. *Phys. Chem. Chem. Phys.* **2019,** *21*, 8434-8444.
(64) Liu, B.; Greeley, J., A Density Functional Theory Analysis of Trends in Glycerol Decomposition on Close-Packed Transition Metal Surfaces. *Phys. Chem. Chem. Phys.* **2013,** *15*, 6475-6485.
(65) Tereshchuk, P.; Chaves, A. S.; Da Silva, J. L. F., Glycerol Adsorption on Platinum Surfaces: A Density Functional Theory Investigation with van der Waals Corrections. *J. Phys. Chem. C* **2014,** *118*, 15251-15259.
(66) Andersson, K. J.; Calle-Vallejo, F.; Rossmeisl, J.; Chorkendorff, I., Adsorption-Driven Surface Segregation of the Less Reactive Alloy Component. *J. Am. Chem. Soc.* **2009,** *131*, 2404-2407.

(67) Hammer, B.; Norskov, J. K., Why Gold is the Noblest of all the Metals. *Nature* **1995,** *376*, 238-240.
(68) Hammer, B.; Nørskov, J. K., Electronic Factors Determining the Reactivity of Metal Surfaces. *Surf. Sci.* **1995,** *343*, 211-220.

Graphical Abstract